Mechanical identification with the reconditioned equilibrium gap method: Formulation, analysis and comparisons

Rémi Pierre Léo Haustrate, François Hild, Amélie Fau

Mechanical identification with the reconditioned equilibrium gap method: Formulation, analysis and comparisons

Rémi Haustrate[a], François Hild[a], Amélie Fau[a,*]

[a] *Université Paris-Saclay, CentraleSupélec, ENS Paris-Saclay, CNRS LMPS – Laboratoire de Mécanique Paris-Saclay, Gif-sur-Yvette, France*

Abstract

Full-field measurements are used to calibrate material parameters. The Equilibrium Gap Method (EGM), like other identification formulations that use full-field data, has the advantage of being direct for linear behavior and some nonlinearities, thereby being computationally cheaper than iterative methods. However, it has a high sensitivity to measurement uncertainties, which is detrimental when dealing with noisy data. The Reconditioned Equilibrium Gap Method (REGM) has been proposed to mitigate this sensitivity. Reconditioning is revisited in this paper from two viewpoints. First, reconditioning may be analyzed as a way of accounting for displacement uncertainties in the cost function. Second, the reconditioned formulation approximates the optimization problem associated with Finite Element Model Updating (FEMU). Based on these developments, the Sequentially Reconditioned Equilibrium Gap Method (SREGM), i.e., an intermediary between FEMU and REGM, is proposed. It uses REGM results to correct the approximation in a fixed-point scheme. Identification results on synthetic and true experiments show that considering the covariance matrix of measured displacements in the cost function is necessary to obtain good identification results. The analyses give insight into unsuccessful cases and confirm that SREGM provides results closer to FEMU than EGM or REGM.

Keywords: Covariance, Identification, Inverse problem, Equilibrium Gap, Uncertainties

*Corresponding author
Email address: amelie.fau@ens-paris-saclay.fr (Amélie Fau)

1. Introduction

Mechanical modeling and analysis of structures require some knowledge about the material behavior, which is generally described by constitutive equations and their associated parameters. Mechanical tests are carried out to identify those parameters by comparing model predictions to experimental data (e.g., displacement fields). Various identification methods based on displacement measurements have been developed over the years [1, 2, 3]. The scope of the present study is limited to full-field displacement data in quasi-static conditions and performing one identification step per displacement field. Identification routes based on other data provided by accelerometers, optics fibers, strain gauges, or extensometers are not discussed herein.

The Equilibrium Gap Method (EGM), initially introduced to identify damage fields [4], is the focus of this paper. It determines the unknown parameters by minimizing equilibrium residuals. It has the advantage of dealing with a quadratic cost function in linear elasticity, and the drawback of working only for full-field measurements. The presence of bias in the result has been reported [5]. In addition, some tests have shown that they yield identification results with higher uncertainties [6, 7, 8, 9]. To reduce the sensitivity of the method to measurement uncertainties, subsequent work has used the EGM to identify a damage law with a reconditioned formulation [10]. This reconditioned formulation has received less attention and will be further reviewed and discussed herein. The original EGM cost function has also been used for mechanical regularization within both Digital Image Correlation (DIC) [11, 12] and Digital Volume Correlation (DVC) [13, 14, 15] analyses as a penalty term. It was shown that the measurement uncertainties could be significantly lowered thanks to such a mechanical filter [16].

Other identification methods are proposed in the literature. The Virtual Field Method (VFM) [17, 18] is derived from the principle of virtual work. This method, which also requires full-field measurements, is direct because the identification is conducted by solving linear systems. It calls for careful construction of the virtual fields. VFM has similarities with EGM from two perspectives. First, the latter can be formulated as a VFM implementation with specific virtual fields [5]. Second, EGM with a finite-element formulation is equivalent to VFM when finite-element bases are used as virtual fields [19].

Finite Element Model Updating (FEMU) [20, 21, 22] iteratively minimizes norms of differences between simulated and measured displacements, forces, or both over the entire domain or parts of it. The Constitutive Relation Error (CRE) [23, 24] uses another metric and has been applied to DIC experiments [25, 26, 6]. The modified CRE [27] is an alternative that combines the constitutive relation error with experimental data mismatches in the minimized cost function [28, 29, 30, 31].

Integrated Digital Image Correlation (IDIC) minimizes the gray level residuals using simulated displacement fields parameterized by the quantities of interest. The gray level residuals are directly used in the cost function instead of the measured displacement field, combining DIC and identification in a single minimization problem. The kinematic bases were first constructed from closed-form solutions to mechanical problems [32]. Calculating these displacement fields with FE simulations [33] offers the same versatility as FEMU. For instance, IDIC eliminates the trade-off between fine meshes and displacement uncertainties when chaining DIC and FEMU [33, 34]. An integrated approach using the modified CRE has also been proposed [31]. Last, the Reciprocity Gap method uses only boundary measurements of displacements and forces as input. For instance, it has been developed to detect cracks [35, 36, 37].

The three identification methods (i.e., EGM, REGM, and VFM) identify parameters within the domain of measured displacement fields [2]. This constraint arises because they use the measured displacement to probe the equilibrium equations. The latter ones cannot be calculated where the displacements are unknown. Additionally, they require that surface displacement measurements (e.g., obtained with DIC) can only be used with some additional assumptions for the missing (bulk) information, such as a plane stress state.

In a recent review on identification techniques [3], the previous methods have been compared according to their sensitivity to high-frequency fluctuations (referred to as spectral sensitivity) due measurement uncertainties. It has been shown that EGM is very sensitive to measurement uncertainties. In contrast, most other identification methods are less sensitive to measurement uncertainties. Therefore, using EGM coupled with reconditioning only (i.e., REGM) was recommended [10].

In terms of material models, IDIC and FEMU can be employed for any type of behavior. In contrast, REGM is essentially limited to linear elasticity or damage fields. Technically, it could be used with other

models but without the advantage of a quadratic cost function. REGM was applied to damage [10, 38] thanks to the fact that the growth law was written in terms of measured strains. REGM is beneficial as it involves simple optimization problems, and its implementation is much easier than that of IDIC and FEMU.

This work discusses the reconditioning required by the EGM to reduce its sensitivity to measurement uncertainties. Two analyses of the formulation are presented. The first one is based on the propagation of displacement uncertainties. The covariance matrix associated with nodal displacement uncertainties is incorporated in the formulation. By including these uncertainties, the sensitivity to noise is reduced. The second analysis shows that the reconditioned formulation can also be found from the linearization of an equivalent formulation of FEMU. The difference between REGM and FEMU is expressed analytically from this linearization. These analyses lead to the Sequentially Reconditioned Equilibrium Gap Method as an intermediate route between REGM and FEMU. Section 2 describes the standard features of the equilibrium gap method. Section 3 discusses the reconditioning of the cost function and analyzes the formulation. Section 4 first illustrates the approach with multiple synthetic experiments. Particular attention is paid to the influence of uncertainties and model error. A case of application of the method to a biaxial test on a composite material is finally investigated.

2. Equilibrium gap method

The Equilibrium Gap Method (EGM) [4, 39] is based on mechanical equilibrium calculated with a measured displacement field. It is classically used with measured displacement fields essentially using Digital Image Correlation (DIC) or Digital Volume Correlation (DVC) data [40]. However, the EGM could also be employed from displacement fields estimated from any simulation or measurement technique.

2.1. Inverse elastic problem

The EGM is derived from linear elasticitywith the small perturbation assumption. The goal of the EGM is to identify elastic properties from the measured displacement field denoted $\mathbf{u}_m$ by minimizing equilibrium residuals using measured displacement fields. The optimization is performed in a finite element

(FE) framework, which has many advantages for mechanical analyses. The FE equilibrium residual reads

$$\underline{\mathbf{r}}_{\mathbf{f}}(\underline{\mathbf{p}}) = \mathbb{K}(\underline{\mathbf{p}})\ \underline{\mathbf{u}}_m - \underline{\mathbf{f}}. \tag{1}$$

where $\underline{\mathbf{p}}$ is the parameter vector (described below), $\mathbb{K}$ is the associated stiffness matrix, $\underline{\mathbf{u}}_m$ is the vector of measured nodal displacements and $\underline{\mathbf{f}}$ the vector of nodal forces.

The stiffness matrix to identify is expressed as a linear combination of a chosen set of matrices to ensure that the cost function is quadratic, which is the main advantage of the EGM (Section 2.2). For homogeneous materials and using the basis $\{\mathbb{K}_i\}$, the stiffness matrix $\mathbb{K}$ becomes

$$\mathbb{K}(\underline{\mathbf{p}}) = \sum_{i=1}^{n_p} c_i\ \mathbb{K}_i, \tag{2}$$

where the basis is defined from the parameters that are searched for. The parameter vector $\underline{\mathbf{p}}$= $[c_1, c_2, ..., c_{n_p}]$ contains n_p quantities corresponding to the size of the chosen basis. Linear decompositions of Hooke's tensor have been presented in previous works [41, 8, 42]; these decompositions can be used as bases. Section 4.1.2 presents the construction of a basis for the identification of isotropic materials under plane stress conditions.

2.2. Optimization problem

The optimization problem aims to minimize the residual forces defined in Equation (1), which linearly depend on the vector of parameters $\underline{\mathbf{p}}$. Therefore, the residual forces are written from the product of a force gradient matrix $\mathbb{L}$ (depending on the measured displacements) and the parameter vector $\underline{\mathbf{p}}$, leading to the following residual

$$\underline{\mathbf{r}}_{\mathbf{f}}(\underline{\mathbf{p}}) = \mathbb{L}(\underline{\mathbf{u}}_m)\ \underline{\mathbf{p}} - \underline{\mathbf{f}} \quad \text{with} \quad \mathbb{L}\left(\underline{\mathbf{u}}\right) = \frac{d\left(\mathbb{K}(\underline{\mathbf{p}})\ \underline{\mathbf{u}}\right)}{d\underline{\mathbf{p}}} = \left[\mathbb{K}_1\underline{\mathbf{u}} \quad ... \quad \mathbb{K}_{n_p}\underline{\mathbf{u}}\right]. \tag{3}$$

The equilibrium residual can be calculated for any parameterization but the matrix $\mathbb{L}$ is constant with respect to $\underline{\mathbf{p}}$ only for linear parameterizations. The residual is minimized with the Euclidean norm $\|\underline{\mathbf{x}}\|_{\mathbb{1}}^2 = \underline{\mathbf{x}}^\top\underline{\mathbf{x}}$. As the minimization is a least-squares problem with an affine transformation, the cost function is quadratic

in $\underline{\mathbf{p}}$.

On some nodes of the finite element mesh, the nodal forces $\underline{\mathbf{f}}$ may be unknown. For instance, for nodes on Dirichlet boundaries or Neumann boundaries with non-zero traction, equilibrium cannot be calculated. Thus, the equilibrium gap cannot be minimized on these nodes. A diagonal matrix $\mathbb{D}$ is used as a mask

$$\underline{\mathbf{r}}_{\mathbf{f},\mathbb{D}}(\underline{\mathbf{p}}) = \mathbb{D}\left(\mathbb{L}(\underline{\mathbf{u}}_m)\underline{\mathbf{p}} - \underline{\mathbf{f}}\right). \tag{4}$$

If all known forces vanish, the scale of $\underline{\mathbf{p}}$ cannot be identified (i.e., if $\underline{\mathbf{p}}$ is a solution, then for any scalar α, vector $\alpha\underline{\mathbf{p}}$ is also a solution to the minimization problem). In addition, using as parameter vector $\alpha\underline{\mathbf{p}}$ shows that minimizing the cost function is achieved with an all-zero parameter vector (i.e., $\alpha = 0$)

$$\left\|\mathbb{D}\mathbb{L}(\underline{\mathbf{u}}_m)\left(\alpha\underline{\mathbf{p}}\right)\right\|_{\mathbb{1}}^2 = \alpha^2\left\|\mathbb{D}\mathbb{L}(\underline{\mathbf{u}}_m)\underline{\mathbf{p}}\right\|_{\mathbb{1}}^2. \tag{5}$$

A constraint is added to the optimization problem to prevent the solution $\underline{\mathbf{p}} = \underline{\mathbf{0}}$. For stiffness fields, one may prescribe their mean [43]. The constraint is chosen depending on the material properties and their parameterization. The general form of the optimization problem that provides $\underline{\mathbf{p}}_{EGM}$, with all possible linear constraints, finally reads

$$\begin{aligned} \min_{\underline{\mathbf{p}}} \quad & \|\mathbb{D}\left(\mathbb{L}(\underline{\mathbf{u}}_m)\underline{\mathbf{p}} - \underline{\mathbf{f}}\right)\|_{\mathbb{1}}^2 \\ \text{subject to} \quad & \mathbb{H}\underline{\mathbf{p}} = \underline{\mathbf{h}} \quad \text{and} \quad \mathbb{G}\underline{\mathbf{p}} \succeq \underline{\mathbf{0}}. \end{aligned} \tag{6}$$

The n_H equality constraints are denoted $\mathbb{H}\underline{\mathbf{p}} = \underline{\mathbf{h}}$, where $\underline{\mathbf{h}}$ is a vector of size n_H and $\mathbb{H}$ a matrix of size $n_H \times n_p$. If $\mathbb{D}\underline{\mathbf{f}}$ is a zero vector, the system $(\mathbb{H}, \underline{\mathbf{h}})$ includes the constraint excluding $\underline{\mathbf{p}} = \underline{\mathbf{0}}$. In addition, inequality constraints, which also depend on the parameterization, may be added to ensure the validity of the parameters when required (e.g., Young's moduli are positive). Assuming these inequalities are linear, they are denoted as $\mathbb{G}\underline{\mathbf{p}} \succeq \underline{\mathbf{0}}$, where $\mathbb{G}$ is a matrix and $\succeq$ enforces that every component of vector $\mathbb{G}\underline{\mathbf{p}}$ must be greater than its right-hand-side counterpart.

With no inequality constraint, the problem is solved directly from the Karush-Kuhn-Tucker equivalent linear system, but the results may be invalid as the inequalities are not necessarily satisfied. The trade-off

between the simplicity of the unconstrained optimization (with no inequalities) and the technicalities of the constrained optimization (with inequalities) ensuring their validity are alleviated by the fact that active-set optimization algorithms already have a mechanism to check whether the inequalities are necessary [44].

The identified parameters using the EGM suffer from the double differentiation of the displacement field in the discrete equilibrium equations (through the stiffness matrix $\mathbb{K}$ [10, 3]). This double differentiation causes the minimized quantity (1) to be sensitive to high-frequency displacement fluctuations and thus to measurement uncertainties [3]. A reconditioned version was thus proposed.

3. Reconditioning

The reconditioning of the EGM [10] was introduced to reduce the effect of displacement uncertainties. It consists in multiplying the equilibrium residual with a reconditioning matrix to transform the cost function. The reconditioned formulation may be constructed from different approaches.

3.1. Reconditioning as an integration

A first reconditioning method has been proposed by using the inverse stiffness matrix of an undamaged material (in the context of damage field identification) [10]. It can be generalized to other situations by choosing arbitrary material properties and constructing the associated inverse stiffness matrix. In either case, multiplying the equilibrium residual by the constructed matrix acts as a double integration that mitigates uncertainty sensitivities.

The stiffness matrix alone is not invertible. Instead, the matrix of the elastic problem with zero Dirichlet boundary conditions where the nodal forces are unknown is used. The associated system becomes

$$\begin{cases} \mathbb{K}\underline{\mathbf{u}} + (\mathbb{1} - \mathbb{D})^\top \underline{\lambda} & = \underline{\mathbf{f}} \\ (\mathbb{1} - \mathbb{D})\underline{\mathbf{u}} & = \underline{\mathbf{0}} \end{cases} \tag{7}$$

where $\underline{\lambda}$ is the vector of Lagrange multipliers used to enforce the Dirichlet boundary conditions. The reconditioning matrix $\mathbb{S}_0$ is the part of the sub-matrix associated with $\underline{\mathbf{u}}$ of the inverse matrix of system (7).

In addition, the diagonal matrix $\mathbb{D}$, defined previously as a mask, is unnecessary with this choice. The inversion of the matrix of the elastic problem yields the reconditioning matrix $\mathbb{S}_0$. The general optimization problem to identify $\underline{\mathbf{p}}_{REGM}$ then becomes

$$\begin{aligned} \min_{\underline{\mathbf{p}}} \quad & \| \mathbb{S}_0 \left(\mathbb{L}(\underline{\mathbf{u}}_m)\underline{\mathbf{p}} - \underline{\mathbf{f}} \right) \|_{\mathbb{1}}^2 \ . \\ \text{subject to} \quad & \mathbb{H}\underline{\mathbf{p}} = \underline{\mathbf{h}} \quad \text{and} \quad \mathbb{G}\underline{\mathbf{p}} \succeq \underline{\mathbf{0}} \end{aligned} \tag{8}$$

It may be interpreted as finding the parameter vector $\underline{\mathbf{p}}$ for which, with the chosen Dirichlet boundaries, the norm of the displacement field created by the residual forces is minimal. The residual forces are the equilibrium error of the elastic problem using the parameters $\underline{\mathbf{p}}$ and the measured displacement $\underline{\mathbf{u}}_m$. This modification of the optimization problem removes the uncertainty sensitivity and makes the reconditioned equilibrium gap similar to FEMU with respect to its spectral sensitivity [3]. It is worth noting that the construction of the reconditioning matrix is computationally expensive because of the inversion of a full matrix. Yet, it is independent of the measured displacements. Therefore, the reconditioning matrix is only built once for many displacement fields.

3.2. Reconditioning as a least-squares covariance weighting

Another advantage of reconditioning lies in the uncertainty propagation of the force residual. For example, the displacement uncertainty is Gaussian for cases where the displacement field is measured by DIC with a white Gauss noise hypothesis on acquired images, and the covariance matrix $\mathbb{C}_u$ associated with nodal displacement uncertainties is known by multiplying the acquisition noise variance with the inverse of the DIC Hessian matrix [45].

The minimized quantity is the residual forces $\underline{\mathbf{r}}_{\mathbf{f}}$ defined in Equation (1), which are linear with respect to the displacement field. Thus, with Gaussian uncertainties for the nodal displacements, the uncertainty on the identified forces follows a correlated Gaussian distribution. If there is no model error, with $\underline{\mathbf{p}}_{ref}$ the true properties of the material, the final residual reduces to noise. Considering the equilibrium residual as

a Gaussian random vector then leads to

$$\underline{\mathbf{r}}_{\mathbf{f}} \sim \mathcal{N}\left(\underline{\mathbf{0}},\ \mathbb{C}_{\underline{\mathbf{r}}_{\mathbf{f}}}(\underline{\mathbf{p}}_{ref}) = \mathbb{K}(\underline{\mathbf{p}}_{ref})\mathbb{C}_u\mathbb{K}(\underline{\mathbf{p}}_{ref})^{\top}\right), \tag{9}$$

where $\mathcal{N}$ denotes the multivariate distribution defined by its mean vector and its covariance matrix. If there is a model error, $\mathbb{K}(\underline{\mathbf{p}})$ cannot accurately describe the measured displacement, the mean value of $\underline{\mathbf{r}}_{\mathbf{f}}$ will not be equal to $\underline{\mathbf{0}}$, and the force residuals will be higher than expected. By associating a random distribution with the equilibrium residual, the parameter $\underline{\mathbf{p}}$ is identified by maximizing the likelihood $P\left(\underline{\mathbf{r}}_{\mathbf{f}}(\underline{\mathbf{p}})\right)$. However, the covariance matrix previously defined is not a full-rank matrix because rigid-body motions lead to the rank deficiency of the stiffness matrix. Therefore, an invertible approximation $\widetilde{\mathbb{C}}_{\underline{\mathbf{r}}_{\mathbf{f}}}(\underline{\mathbf{p}})$ needs to be built to calculate the probability density function

$$P\left(\underline{\mathbf{r}}_{\mathbf{f}}(\underline{\mathbf{p}})\right) = \frac{\exp\left(-\frac{1}{2}\|\underline{\mathbf{r}}_{\mathbf{f}}(\underline{\mathbf{p}})\|^2_{\mathbb{C}^{-1}_{\underline{\mathbf{r}}_{\mathbf{f}}}(\underline{\mathbf{p}})}\right)}{\sqrt{(2\pi)^{n_r}\det\left(\widetilde{\mathbb{C}}_{\underline{\mathbf{r}}_{\mathbf{f}}}(\underline{\mathbf{p}})\right)}} \tag{10}$$

with

$$\|\underline{\mathbf{r}}_{\mathbf{f}}\|^2_{\mathbb{C}^{-1}_{\underline{\mathbf{r}}_{\mathbf{f}}}(\underline{\mathbf{p}})} := \left(\mathbb{K}(\underline{\mathbf{p}})\underline{\mathbf{u}}_m - \underline{\mathbf{f}}\right)^{\top}\left(\widetilde{\mathbb{C}}_{\underline{\mathbf{r}}_{\mathbf{f}}}(\underline{\mathbf{p}})\right)^{-1}\left(\mathbb{K}(\underline{\mathbf{p}})\underline{\mathbf{u}}_m - \underline{\mathbf{f}}\right). \tag{11}$$

The inversion of the stiffness matrix $\mathbb{K}(\underline{\mathbf{p}})$ is impossible due to rigid-body motions. An elastic problem with Dirichlet boundary conditions can be defined as an alternative problem for which an inverse exists(as in Equation (7)). In the REGM, the choice is to solve an elastic problem with zero-Dirichlet boundary conditions on nodes where nodal forces are not zero. The inverse matrix of this problem is denoted as $\mathbb{K}_{\mathbb{D}}(\underline{\mathbf{p}})^{-1}$ and constructed in the same way as $\mathbb{S}_0$ (Equation (7)). The invertible approximation of the covariance matrix is then recast as

$$\widetilde{\mathbb{C}}_{\underline{\mathbf{r}}_{\mathbf{f}}}(\underline{\mathbf{p}}) = \mathbb{K}_{\mathbb{D}}(\underline{\mathbf{p}})\mathbb{C}_u\mathbb{K}_{\mathbb{D}}(\underline{\mathbf{p}})^{\top}. \tag{12}$$

The norm of the force residual based on the covariance (Equation (11)) is rewritten as

$$\|\underline{\mathbf{r}}_{\mathbf{f}}\|^2_{\mathbb{C}^{-1}_{\underline{\mathbf{r}}_{\mathbf{f}}}(\underline{\mathbf{p}})} = \|\mathbb{K}_{\mathbb{D}}(\underline{\mathbf{p}})^{-1}\left(\mathbb{K}(\underline{\mathbf{p}})\underline{\mathbf{u}}_m - \underline{\mathbf{f}}\right)\|^2_{\mathbb{C}_u^{-1}} \tag{13}$$

with the $\mathbb{C}_u^{-1}$-norm defined as

$$\forall\ \underline{\mathbf{u}} \in \mathbb{R}^{n_\varphi} \quad , \quad \|\underline{\mathbf{u}}\|^2_{\mathbb{C}_u^{-1}} = \underline{\mathbf{u}}^\top \mathbb{C}_u^{-1}\underline{\mathbf{u}}. \tag{14}$$

Weighting the norm with the covariance matrix is optimal assuming the uncertainty model is correct [3]. This weighting was also used in the context of parametric [46] or FEMU [47] identification. The quantity inside the $\mathbb{C}_u^{-1}$ norm is not linear with respect to $\underline{\mathbf{p}}$. However, a linear approximation may be constructed by choosing an arbitrary vector $\underline{\mathbf{p}}_0$ to build a fixed inverse matrix

$$\|\underline{\mathbf{r}}_{\mathbf{f}}\|^2_{\mathbb{C}^{-1}_{\underline{\mathbf{r}}_{\mathbf{f}}}(\underline{\mathbf{p}})} \simeq \|\mathbb{K}_{\mathbb{D}}(\underline{\mathbf{p}}_0)^{-1}\left(\mathbb{K}(\underline{\mathbf{p}})\underline{\mathbf{u}}_m - \underline{\mathbf{f}}\right)\|^2_{\mathbb{C}_u^{-1}}. \tag{15}$$

To summarize, with the additional approximation that $\widetilde{\mathbb{C}}_{\underline{\mathbf{r}}_{\mathbf{f}}}(\underline{\mathbf{p}}) \simeq \widetilde{\mathbb{C}}_{\underline{\mathbf{r}}_{\mathbf{f}}}(\underline{\mathbf{p}}_0)$, the maximization of $\log P\left(\underline{\mathbf{r}}_{\mathbf{f}}(\underline{\mathbf{p}})\right)$ results in the minimization of Equation (15), which is equivalent to a reconditioned formulation of the equilibrium gap weighted by $\mathbb{C}_u^{-1}$. The chosen parameter vector $\underline{\mathbf{p}}_0$ represents the undamaged material in the initial formulation. Here, the vector $\underline{\mathbf{p}}_0$ represents an arbitrary choice of material parameters for a homogeneous material.

This formulation explains the reduction of uncertainty sensitivity. The reconditioned method leads to a cost function that is a least-squares minimization with a covariance weighting, i.e., an approximation of the optimal norm in the sense of the maximum likelihood. The link with the maximum likelihood means that the reconditioned cost function includes information about displacement uncertainties from their covariance matrix, which helps to distinguish signal from noise.

3.3. Reconditioning as an approximation of FEMU

FEMU is an identification method that minimizes the difference between simulated and measured displacements [20]. Unlike the equilibrium gap methods, it does not need full-field measurements. However,

it is assumed hereafter that full-field measurements are available. FEMU identifies the parameter vector $\underline{\mathbf{p}}_{\text{FEMU}}$ by minimizing the residual

$$\underline{\mathbf{r}}_u(\underline{\mathbf{p}}) = \underline{\mathbf{u}}_s(\underline{\mathbf{p}}) - \underline{\mathbf{u}}_m \tag{16}$$

between measured nodal displacements $\underline{\mathbf{u}}_m$ and the solution to a finite-element simulation $\underline{\mathbf{u}}_s(\underline{\mathbf{p}})$

$$\min \|\underline{\mathbf{u}}_s(\underline{\mathbf{p}}) - \underline{\mathbf{u}}_m\|^2_{\mathbb{C}_u^{-1}} \tag{17}$$

using the norm (14) that weights the difference using the covariance matrix. Appendix A presents the construction of the optimal residual covariance matrix, which includes measurement uncertainties associated with measured boundary conditions [5]. It is not considered hereafter for the sake of simplicity.

Assuming a linear elastic behavior, the FE simulation is expressed as a linear system of equations, which comprises the discretized weak form of the equilibrium equation and the Dirichlet boundary conditions enforced, e.g., via Lagrange multipliers

$$\begin{cases} \mathbb{K}(\underline{\mathbf{p}})\underline{\mathbf{u}}_s(\underline{\mathbf{p}}) + \mathbb{A}^\top \underline{\lambda}_s(\underline{\mathbf{p}}) & = \underline{\mathbf{f}} \\ \mathbb{A}\underline{\mathbf{u}}_s(\underline{\mathbf{p}}) & = \mathbb{A}\underline{\mathbf{u}}_m \end{cases} \tag{18}$$

with $\underline{\lambda}_s$ the Lagrange multipliers, and $\mathbb{A}$ a projection matrix that extracts the nodal displacements that are on Dirichlet boundaries from vectors $\underline{\mathbf{u}}_s$ and $\underline{\mathbf{u}}_m$. Using the nodes where the forces are unknown to prescribe Dirichlet boundary conditions allows one to express $\mathbb{A}$ with respect to $\mathbb{D}$ (from Equation (4)) as follows $\mathbb{A} = \mathbb{1} - \mathbb{D}$.

The cost function (17) is minimized for identifying the parameters by updating the parameter vector $\underline{\mathbf{p}}$, with no inequality constraints. The update is generally performed using Gauss-Newton's method or an alternative adapted to least-squares problems such as the Levenberg-Marquardt scheme [22, 44].

The REGM also minimizes displacement gaps as the reconditioning matrix transforms the equilibrium residual (i.e., unbalanced forces) into displacements that are solution to an elastic problem with unbal-

anced forces included as body forces. The link between FEMU and REGM is established from the link between these two displacement fields. The REGM residual displacement is defined from the minimization problem (8) as

$$\underline{\mathbf{r}}_{\mathrm{REGM}} := \mathbb{K}_{\mathbb{D}}^{-1}(\underline{\mathbf{p}}_0)\left(\mathbb{K}(\underline{\mathbf{p}})\underline{\mathbf{u}}_m - \underline{\mathbf{f}}\right). \tag{19}$$

As REGM has no simulated displacements to link the two methods, one expresses the FEMU formulation without $\underline{\mathbf{u}}_s$. Thus, $\underline{\mathbf{u}}_s$ is derived from the measured displacement $\underline{\mathbf{u}}_m$ and the residual displacement $\underline{\mathbf{r}}_{\mathbf{u}}$

$$\underline{\mathbf{u}}_s(\underline{\mathbf{p}}) = \left(\underline{\mathbf{u}}_s(\underline{\mathbf{p}}) - \underline{\mathbf{u}}_m\right) + \underline{\mathbf{u}}_m = \underline{\mathbf{r}}_{\mathbf{u}}(\underline{\mathbf{p}}) + \underline{\mathbf{u}}_m. \tag{20}$$

The linear system (18) is rewritten using the previous equation

$$\begin{cases} \mathbb{K}(\underline{\mathbf{p}})\left(\underline{\mathbf{r}}_{\mathbf{u}}(\underline{\mathbf{p}}) + \underline{\mathbf{u}}_m\right) + \mathbb{A}^{\top}\underline{\lambda}_s(\underline{\mathbf{p}}) & = \underline{\mathbf{f}} \\ \mathbb{A}\left(\underline{\mathbf{r}}_{\mathbf{u}}(\underline{\mathbf{p}}) + \underline{\mathbf{u}}_m\right) & = \mathbb{A}\underline{\mathbf{u}}_m \end{cases} \tag{21}$$

and then, without including the simulated displacement, calculating the FEMU residual displacement $\underline{\mathbf{r}}_{\mathbf{u}}$ is equivalent to solving the following problem

$$\begin{cases} \mathbb{K}(\underline{\mathbf{p}})\underline{\mathbf{r}}_{\mathbf{u}}(\underline{\mathbf{p}}) + \mathbb{A}^{\top}\underline{\lambda}_s(\underline{\mathbf{p}}) & = \underline{\mathbf{f}} - \mathbb{K}(\underline{\mathbf{p}})\underline{\mathbf{u}}_m \\ \mathbb{A}\underline{\mathbf{r}}_{\mathbf{u}}(\underline{\mathbf{p}}) & = \underline{\mathbf{0}} \end{cases} \tag{22}$$

where $\underline{\lambda}_s(\underline{\mathbf{p}})$ denotes the Lagrange multipliers introduced in Equation (18). After choosing an arbitrary parameter vector $\underline{\mathbf{p}}_0$, the stiffness matrix on the right-hand side is replaced by that built from $\underline{\mathbf{p}}_0$, making the matrix to be inverted independent of $\underline{\mathbf{p}}$. The problem is thus recast as

$$\begin{cases} \mathbb{K}(\underline{\mathbf{p}}_0)\underline{\mathbf{r}}_{\mathbf{u}}(\underline{\mathbf{p}}) + \mathbb{A}^{\top}\underline{\lambda}_s(\underline{\mathbf{p}}) & = \underline{\mathbf{f}} - \mathbb{K}(\underline{\mathbf{p}})\underline{\mathbf{u}}_m - \left(\mathbb{K}(\underline{\mathbf{p}}) - \mathbb{K}(\underline{\mathbf{p}}_0)\right)\underline{\mathbf{r}}_{\mathbf{u}}(\underline{\mathbf{p}}) \\ \mathbb{A}\underline{\mathbf{r}}_{\mathbf{u}}(\underline{\mathbf{p}}) & = \underline{\mathbf{0}}. \end{cases} \tag{23}$$

Last, an approximation is made by ignoring the right-hand-side term, which depends on $\underline{\mathbf{r}}_{\mathbf{u}}$. Therefore, the FEMU residual calculation is approximated by the following system

$$\begin{cases} \mathbb{K}(\underline{\mathbf{p}}_0)\underline{\mathbf{r}}_{\mathbf{u}}(\underline{\mathbf{p}}) + (\mathbb{1}-\mathbb{D})^{\top}\underline{\lambda}_s(\underline{\mathbf{p}}) & \simeq \underline{\mathbf{f}} - \mathbb{K}(\underline{\mathbf{p}})\underline{\mathbf{u}}_m \\ (\mathbb{1}-\mathbb{D})\,\underline{\mathbf{r}}_{\mathbf{u}}(\underline{\mathbf{p}}) & = \underline{\mathbf{0}}, \end{cases} \tag{24}$$

which can be inverted. Only the right-hand side depends on the parameter vector $\underline{\mathbf{p}}$. Precomputing the inverse matrix of the system gives access to the reconditioning matrix $\mathbb{S}_0$ used in REGM (8) because $\mathbb{A}$ has been chosen to be $\mathbb{A} = \mathbb{1} - \mathbb{D}$ i.e., the nodes used for the Dirichlet boundary conditions are those where the forces are not vanishing. The displacement residual $\underline{\mathbf{r}}_{\mathbf{u}}$ calculated from this approximation is equivalent to the displacement residual inside the cost function (15) obtained for the REGM, and thus to the displacement minimized in the REGM. The term removed for the approximation of the FEMU residual (24) reads

$$\left(\mathbb{K}(\underline{\mathbf{p}}) - \mathbb{K}(\underline{\mathbf{p}}_0)\right)\underline{\mathbf{r}}_{\mathbf{u}}\left(\underline{\mathbf{p}}\right). \tag{25}$$

The approximation error is small if $\underline{\mathbf{r}}_{\mathbf{u}}\left(\underline{\mathbf{p}}\right)$ is small, or if the initial guess $\underline{\mathbf{p}}_0$ is close to the parameter $\underline{\mathbf{p}}$ used for the simulation. If there is no model error, the residual $\underline{\mathbf{r}}_{\mathbf{u}}$ only contains displacement measurement uncertainties when the optimization has converged. The formulations associated with FEMU and REGM for full-field measurements are thus explicitly linked as the REGM residual is equivalent to a linearization of the FEMU kinematic residual

$$\underline{\mathbf{r}}_{\mathbf{u}}(\underline{\mathbf{p}}) \;\simeq\; \mathbb{K}_{\mathbb{D}}^{-1}(\underline{\mathbf{p}}_0)\left(\underline{\mathbf{f}} - \mathbb{K}(\underline{\mathbf{p}})\underline{\mathbf{u}}_m\right) = -\underline{\mathbf{r}}_{\mathrm{REGM}}(\underline{\mathbf{p}}). \tag{26}$$

Provided there is no model error and the uncertainties on the measured displacement are low, at the minimum $\underline{\mathbf{p}}_{FEMU}$ of the FEMU cost function (17), the residual $\underline{\mathbf{r}}_{\mathbf{u}}$ will be small. For parameters close to $\underline{\mathbf{p}}_{FEMU}$, the approximation (26) holds and the REGM cost function (8) is close to the FEMU cost function. Thus, the REGM has a solution $\underline{\mathbf{p}}_{REGM}$ close to $\underline{\mathbf{p}}_{FEMU}$, making the two methods similar.

The derivations of the reconditioning as an integration or as a least-squares covariance weighting are based on arbitrary approximations. The uncertainty sensitivity reduction was substantiated without explicitly quantifying the effect of these approximations. For the reconditioning formulation based on FEMU, the approximation compared with the FEMU formulation was carried out by neglecting a term in the mechanical linear system, and thus, it was quantified. This quantification showed that with low displacement uncertainties and no model error, REGM and FEMU yielded similar results.

3.4. Sequentially reconditioned formulation (SREGM)

The REGM performs as well as FEMU with low displacement uncertainties and no model error (see Equation (25)). However, many experiments deal with non-negligible displacement uncertainties or samples with complex mechanical behavior, thereby leading to model errors in the identification procedure. In these cases, the choice of $\underline{\mathbf{p}}_0$ in the REGM procedure has an undesirable effect on the identification results, assuming the reference identification method is FEMU. An explicit interpretation is given to the method parameter $\underline{\mathbf{p}}_0$ of the optimization procedure as it represents a specific Hooke's tensor. Thus, its choice may be driven by physical knowledge. As demonstrated in the previous section, its effect on the identification results can be reduced if its value is close to the optimized result $\underline{\mathbf{p}}_{\text{REGM}}$.

The Sequentially Reconditioned Equilibrium Gap Method (SREGM) is proposed to reduce the impact of the reconditioning parameter $\underline{\mathbf{p}}_0$ on the identification result. The function of REGM $(\underline{\mathbf{u}}, \underline{\mathbf{p}}_0) \rightarrow \underline{\mathbf{p}}_{\text{REGM}}$ takes a displacement field $\underline{\mathbf{u}}$ and a reconditioning parameter $\underline{\mathbf{p}}_0$ as input and returns the optimization result $\underline{\mathbf{p}}_{\text{REGM}}$. The idea behind SREGM is to find the parameter vector $\underline{\mathbf{p}}_{\text{SREGM}}$ such that the equality

$$\underline{\mathbf{p}}_{\text{SREGM}} = \text{REGM}(\underline{\mathbf{u}}_m, \underline{\mathbf{p}}_{\text{SREGM}}) \tag{27}$$

is satisfied. Therefore, SREGM corresponds to a fixed-point problem that can be solved iteratively. At iteration k of SREGM, the REGM is used to estimate a new optimum as

$$\underline{\mathbf{p}}^*_{k+1} \leftarrow \text{REGM}(\underline{\mathbf{u}}_m, \underline{\mathbf{p}}^*_k) \tag{28}$$

until the iterative algorithm stops when the convergence criterion is reached. A simple criterion is

$$\|\underline{\mathbf{p}}^*_{k+1} - \underline{\mathbf{p}}^*_k\|_{\underline{\mathbf{p}}} \leq \|\underline{\mathbf{p}}^*_{k+1}\|_{\underline{\mathbf{p}}} \times 10^{-n} \tag{29}$$

with $\|.\|_{\underline{\mathbf{p}}}$ a norm for the parameter space and n a user-chosen threshold parameter. Thus, the SREGM scheme alternates REGM identification and updates of the reconditioning matrix with the currently identified parameter vector. The qualifier "sequentially" is chosen because of the parallel with the Sequential quadratic programming optimization algorithm, which solves a nonlinear optimization problem with a series of quadratic programming optimizations [44]. The SREGM is thus seen as an intermediary between REGM and FEMU.

REGM has computational advantages compared to FEMU. REGM is a linear constrained least-squares problem, whereas FEMU generally is a nonlinear least-squares constrained problem. It is still to be determined whether SREGM keeps the advantages of REGM as it is a linear constrained least-squares problem inside a fixed point iterative scheme.

Even if the construction of the reconditioning matrix needs a full inversion, which is computationally expensive, REGM is a relatively low-cost approach because the reconditioning matrix is built only once and then used for any number of identifications based on the same FE mesh. The sequential process may a priori lose this advantage because each fixed-point iteration needs a new reconditioning matrix to be constructed. Multiple ways may be explored to restrict the number of reconditioning matrices to build and control the increase in numerical cost. Reducing the number of fixed-point iterations will proportionally reduce the number of constructions. Thus, convergence acceleration [48] could be adequate. Here, a surrogate model is proposed, which is easy to implement for identifying a small number of parameters. It directly prevents one from repeatedly building reconditioning matrices as long as the surrogate model is accurate enough.

The fixed-point problem is solved using a surrogate model $M_{\underline{\mathbf{u}}}$, which aims to calculate quickly an approximation of the identified parameters $\widehat{\underline{\mathbf{p}}}_{REGM}$ knowing a reconditioning parameter $\underline{\mathbf{p}}_0$ and a given displacement field. The model $M_{\underline{\mathbf{u}}}$ approximates $\widehat{\underline{\mathbf{p}}}_{REGM}$ for any reconditioning parameter $\underline{\mathbf{p}}_0$ and a given

displacement field $\underline{\mathbf{u}}$ from a few data points. The advantage of this approach is that a small number of reconditioning matrices is used to build the surrogate model of any number of displacement fields. The reuse of each matrix reduces the computational cost. The more displacement fields are exploited, the higher the interest in the SREGM approach. After convergence in parameters has been reached, the SREGM result and its convergence are checked directly using REGM as an additional iteration.

In Section 4, this method is used to identify the Poisson ratio. In that simple case, the chosen surrogate model is a low-order polynomial obtained by linear regression. The surrogate strategy is a pillar of SREGM, but any technique (e.g., interpolation) can be employed for building it. REGM may generate an excellent initial guess for FEMU. This guess would help reduce the number of FEMU to benefit from two advantages, namely, low computational cost of REGM, and the FEMU cost function that does not have $\underline{\mathbf{p}} = \underline{\mathbf{0}}$ as a solution. The choice of the best numerical strategy is not obvious; it will not be studied herein.

4. Application to the identification of Poisson's ratio

The previous methods are applied to an equibiaxial test on a composite material, which has been described in Refs. [4, 1, 10, 33]. Reference results are available for the Young's modulus and Poisson's ratio [1, 33]. The parameter of interest is the Poisson's ratio ν as it is very challenging for identification procedures. From a previous work, a value of 0.31 is expected [33]. It is worth noting that the mechanical test was not designed for the identification of the Poisson's ratio. First, the experiment and the parameterization of the Hooke's tensor are introduced. Then, results for multiple synthetic experiments are presented and analyzed. Last, the identification is performed with experimental data.

4.1. Experiment and identification framework

This section describes the features for identifying the Poisson's ratio for synthetic and real tests. First, the specimen and loading of the real experiment are described, along with some preliminary analyses. These analyses are fundamental as the synthetic experiments are constructed from the real experiment. The material parameterization for the identification is given. Last, the different identification methods and the quantities used to assess them are presented.

4.1.1. Experimental data

The sample (Figure 1) has a cross-shaped geometry. The length of the sides is 36.5 mm, and the radius of curvature is 5 mm. The thickness is 3 mm. The material is a vinylester matrix reinforced by E-glass fibers randomly oriented with a quasi-uniform distribution, thereby ensuring a quasi-isotropic behavior for the in-plane response. The material was tested with unnotched and notched specimens in uniaxial tension [49]. For the experiment used herein, an equibiaxial load with a force amplitude F was applied. The experimental data consist of a reference image I_0 with no applied load (Figure 1(a)) and 11 images I_1 to I_{11} acquired every kN from 1 to 11 kN. The failure of the sample was reached just after 11 kN. Each image has a definition of 1016×1008 px. The physical size of one pixel (px) is 68 µm. Plane stress conditions are assumed.

The displacement field is discretized on an FE mesh made of triangular elements with piecewise linear shape functions (Figure 1(b)). The mesh comprises 1,936 nodes and 3,700 elements of mean characteristic length equal to 13.8 px (or 94 µm). Figure 1(b) shows the mask applied to the nodes; yellow indicates nodes where the mask is equal to 1, and blue indicates non-free boundaries (i.e., nodes where the mask is equal to 0). Dirichlet boundary conditions with measured displacements are prescribed on every node whose mask is equal to zero; they are not accounted for in the equilibrium residual minimization as the equilibrium cannot be calculated for them. The number of equilibrium equations is 3,652.

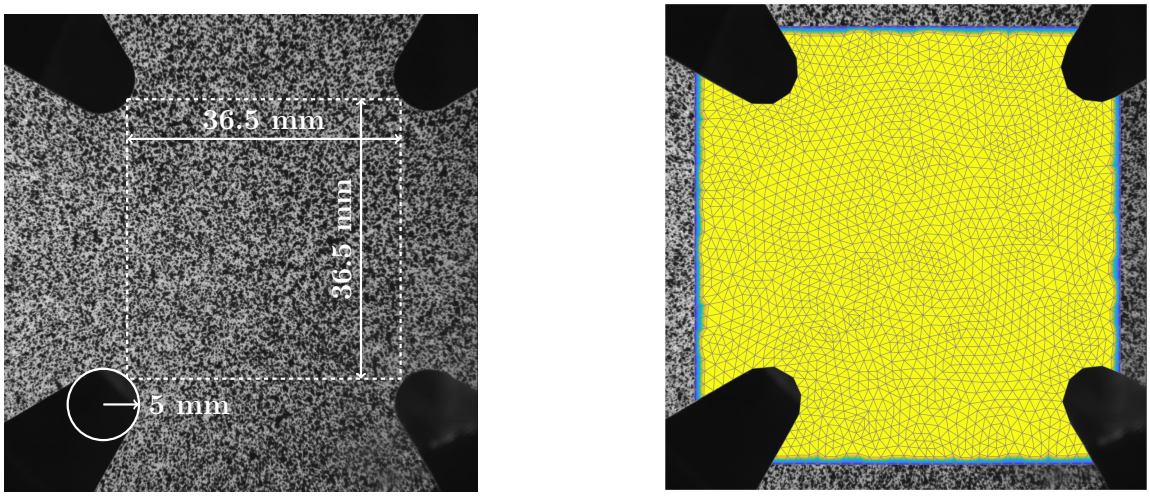

(a) (b)

Figure 1: Cross-shaped specimen subjected to an equibiaxial loading. (a) Reference image I_0. (b) Sample and FE mesh. The color represents the mask used for evaluating the equilibrium residual: yellow indicates nodes where the equilibrium is evaluated and is minimized; blue depicts (Dirichlet) nodes where the equilibrium is unknown.

Figure 2 shows the average strains along the two loading directions as functions of the applied force. The strain averages are calculated using the DIC measured displacements over the whole domain Ω, weighted by the element size. The strain levels are different in both directions, which may be explained by elastic anisotropy [1, 50], and for the last loading steps, by the presence of damage, namely, the material degradation inducing a reduction of the stiffness of the material [51] (Figure 3).

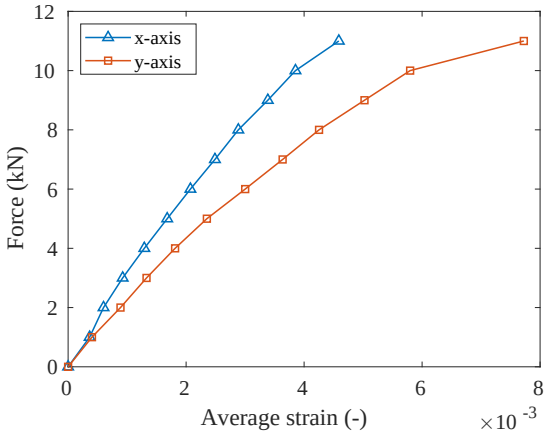

Figure 2: Average strain $\langle \epsilon_{xx} \rangle$ and $\langle \epsilon_{yy} \rangle$ vs. force of the studied equibiaxial experiment on a cross-shaped sample (Figure 1(a)).

When $F = 6$ kN, the maximum principal strains concentrate on the curved free boundaries (Figure 3(a)).

Very high values are observed near the connecting radii and along the crack mouth when $F = 11$ kN (Figure 3(b)).

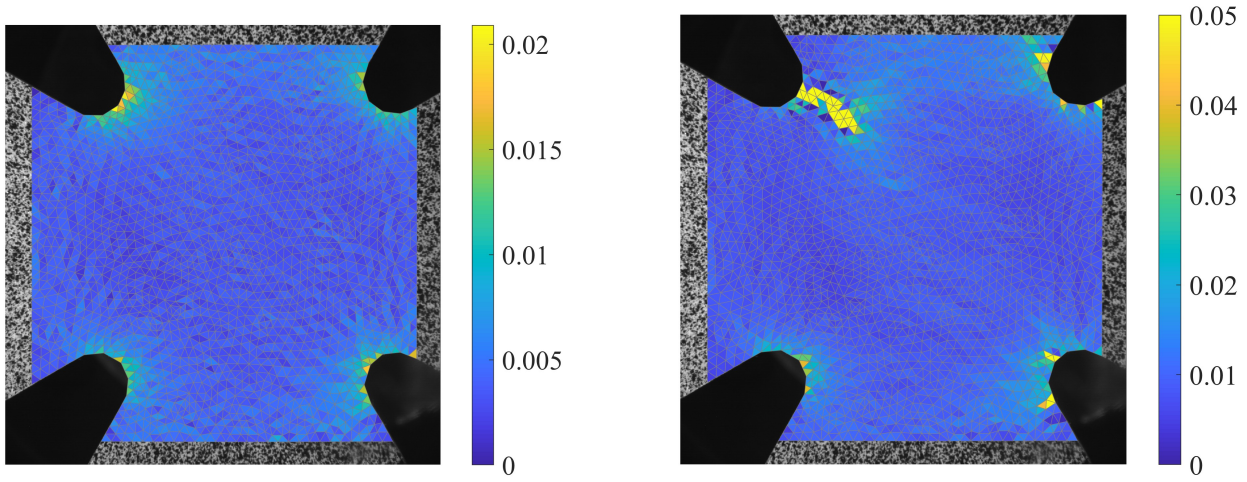

Figure 3: Maximum principal strain fields calculated from DIC measured displacements when $F = 6$ kN (a) and $F = 11$ kN (b). The strain scale of sub-figure (b) is limited to a level of 0.05 for the sake of readability. Strains whose level does not lie within the selected range are shown with a saturated hue. They are located in the elements traversed by cracks.

The acquisition noise level of the images is estimated from the gray level residuals associated with the registration of image I_1, which corresponds to the lowest displacement amplitudes. The covariance matrix $\mathbb{C}_u$ associated with displacement uncertainties is calculated with the inverse of the DIC Hessian matrix [45]. The norm $\|\bullet\|_{\mathbb{C}_u^{-1}}$ in Equation (14) is employed for estimating global displacement residuals. In addition, $\mathbb{C}_u$ is utilized to generate simulated displacements with their uncertainties and correlations instead of assuming uncorrelated Gaussian white noise, which would be equivalent to approximating $\mathbb{C}_u$ as proportional to the identity matrix.

Multiple methods have been developed to specifically investigate crack propagation with DIC [52, 53]. In the following, the identified model is not intended to represent damage nor cracks. The focus is put on the features and performances of the EGM for challenging cases. The identification results after damage has initiated only give insight into the robustness of the identification procedures for handling model errors.

4.1.2. Linear parameterization for plane stress isotropic elasticity

The linearity of the force residuals depends on the dependence of Hooke's tensor on the parameters to identify. Therefore, the identification of the Poisson ratio ν cannot be directly performed because the force residuals are nonlinear with respect to ν. Hooke's law is expressed linearly with respect to Lamé's coefficients λ and μ in 3D situations. However, Hooke's tensor does not depend linearly on these coefficients under a plane stress assumption. This section presents one way to have a linear parameterization of the plane stress Hooke's tensor. Another parameterization based on a spectral decomposition of Hooke's tensor may be used [8]. It is detailed in Appendix B, where it is compared to the previous parameterization based on a linear interpolation.

A stiffness tensor associated with any Poisson's ratio can be represented by interpolating two stiffness tensors corresponding to different Poisson's ratios. Besides, for a fixed value of the Poisson's ratio, the isotropic stiffness tensor associated with any value of Young's modulus is represented by scaling the stiffness matrix related to another value of Young's modulus. In the present case, a unitary Young's modulus is chosen for the two basis tensors. The decomposition of the stiffness matrix (Equation (2)) becomes

$$\mathbb{K}(\underline{\mathbf{p}}) = c_{0.5}\mathbb{K}_{0.5} + c_0\mathbb{K}_0 \quad \text{with} \quad \underline{\mathbf{p}} = \begin{bmatrix} c_{0.5} \\ \\ c_0 \end{bmatrix} \tag{30}$$

where $\mathbb{K}_{0.5}$ is the stiffness matrix of an incompressible and isotropic material (i.e., $\nu = 0.5$), and $\mathbb{K}_0$ that of an isotropic material with $\nu = 0$. The coefficients $\underline{\mathbf{p}}$ represent the contribution of each case. Appendix B presents how to calculate E and ν from $\underline{\mathbf{p}}$ and the inequalities on $\underline{\mathbf{p}}$ that allows for valid values.

With no force data, the solution $\underline{\mathbf{p}} = \underline{\mathbf{0}}$ is possible, and thus the Young's modulus is not identifiable. A constraint needs to be added to the optimization problem. Prescribing one value to the Young's modulus leads to a nonlinear constraint. Transforming the problem into a linear interpolation between the two materials characterized by $\mathbb{K}_{0.5}$ and $\mathbb{K}_0$ is an alternative for not losing the computational advantages of

linear constraints. The constraint is chosen to be

$$c_{0.5} + c_0 = 1. \tag{31}$$

4.1.3. Features of the identification methods

The identification of the Poisson's ratio is conducted for each measured displacement field with the raw equilibrium gap formulation (EGM), the reconditioned version (REGM), and the sequentially reconditioned method (SREGM). With the same parameterization, an identification with FEMU has also been carried out for comparison purposes.

The optimization problem for the equilibrium gap, which yields $\underline{\mathbf{p}}_{\text{EGM}}$ reads

$$\begin{aligned} \min_{\underline{\mathbf{p}}} \quad & \|\mathbb{D}\mathbb{L}(\mathbf{u}_m)\underline{\mathbf{p}}\|^2_{\mathbb{M}} \\ \text{subject to} \quad & c_{0.5} + c_0 = 1 \quad \text{and} \quad \mathbb{G}\underline{\mathbf{p}} \succcurlyeq \underline{\mathbf{0}} \end{aligned} \tag{32}$$

where $\mathbb{D}$ is the matrix that discards the equilibrium equations that are not known, and $\mathbb{G}$ the matrix accounting for the parameter inequalities (see Appendix B, Equation (50)). To take into account the fact that the FE mesh may have elements of different sizes, the metric used for minimization is constructed from the $\mathcal{L}^2$ norm on the domain Ω

$$\forall\ \underline{\mathbf{u}} = [u_1\ u_2\ ...\ u_{n_\varphi}]^\top \quad , \quad \|\underline{\mathbf{u}}\|^2_{\mathbb{M}} = \underline{\mathbf{u}}^\top \mathbb{M} \underline{\mathbf{u}} = \int_\Omega \left(\sum_{i=1}^{n_\varphi} u_i \boldsymbol{\varphi}_i \right) \cdot \left(\sum_{j=1}^{n_\varphi} u_j \boldsymbol{\varphi}_j \right) d\Omega \tag{33}$$

where $\boldsymbol{\varphi}_i$ are the (vectorial) FE shape functions, and $\mathbb{M}$ corresponds to a mass matrix.

The reconditioned formulation needs a reconditioning parameter vector $\underline{\mathbf{p}}_0$ to calculate the approximate inverse stiffness matrix $\mathbb{S}_0$. As shown in Section 3, $\underline{\mathbf{p}}_0$ should be as close as possible to the actual material parameter of the sample. Thus, in general, any prior knowledge about the material is beneficial to choose $\underline{\mathbf{p}}_0$. With the multiple identifications performed hereafter, the value of $\underline{\mathbf{p}}_0$ could be updated between the different application cases. In addition, for the synthetic cases, the best $\underline{\mathbf{p}}_0$ can be predicted. However, for

the sake of comparison, only one reconditioning parameter vector $\underline{\mathbf{p}}_0$, which is $c_{0.5} = c_0 = 0.5$ corresponding to $\nu_0 = 0.29$ according to Equation (49), is employed for all cases.

The optimization of the reconditioned formulation, which gives $\underline{\mathbf{p}}_{\text{REGM}}$, has the same constraints, but the cost function reduces to

$$\|\mathbb{S}_0\mathbb{L}(\underline{\mathbf{u}}_m)\underline{\mathbf{p}}\|^2_{\mathbb{C}_u^{-1}} \tag{34}$$

where the norm uses the inverse covariance matrix $\mathbb{C}_u^{-1}$ as metric. As the used least-squares optimization solver works with the euclidean norm $\| \bullet \|^2_{\mathbb{1}}$, the norm associated with the metric $\mathbb{C}_u^{-1}$ is implemented by multiplying the vector of interest by a matrix equivalent to the square-root of $\mathbb{C}_u^{-1}$. This matrix can be constructed from the eigenvalue decomposition $\mathbb{C}_u^{-1} = \mathbb{P}\mathbb{V}\mathbb{P}^\top$

$$\forall \underline{\mathbf{r}}, \quad \|\underline{\mathbf{r}}\|^2_{\mathbb{C}_u^{-1}} = \|\sqrt{\mathbb{V}}\mathbb{P}^\top\underline{\mathbf{r}}\|^2_{\mathbb{1}} = \underline{\mathbf{r}}^\top\mathbb{C}_u^{-1}\underline{\mathbf{r}}. \tag{35}$$

It is worth noting that the Cholesky factorization $\mathbb{C}_u^{-1} = \mathbb{U}_{\underline{\mathbf{u}}}^\top\mathbb{U}_{\underline{\mathbf{u}}}$ can also be used and yields an equivalent norm with reduced computational cost.

SREGM identification is accelerated with the surrogate approach introduced in Section 3.4. This identification route has the advantage of involving only one parameter. Thus, a simple function $M_u : \nu_0 \mapsto \nu_{REGM}$ is used as the surrogate model, as it is not constrained to a linear parameterization. A polynomial of degree 2 is constructed by linear regression from 10 REGM identifications, which are performed with different values of ν_0. This simple surrogate model allows one to solve the fixed-point problem by finding the roots of a polynomial. After solving the SREGM problem with the surrogate, a last identification step is performed by REGM with an updated reconditioning matrix. The surrogate model solution and the updated REGM solution are compared to check that the surrogate model has not introduced errors. The criterion is that the change in ν is less than 0.01 in absolute value. The degree and the number of observation points are empirical.

For the FEMU method, the cost function (17) is minimized. The equality constraint (31) is not necessary with FEMU because the method updates the simulated displacements using the displacement sensitivity

to the parameters of interest. Synthetic experiments show that adding the linear constraint (31) (or the nonlinear constraint $E = 1$) reduces the required number of iterations and the computational time.

All linear least-squares problems are solved with Matlab's solver `lsqlin` using default stopping criteria and the active-set algorithm [54]. Nonlinear least squares minimizations (e.g., FEMU) are carried out with the `lsqnonlin` solver with stopping criteria identical to those used in `lsqlin` and the interior-point algorithm [55].

4.1.4. Identification residuals

Several identification residuals can be constructed to assess results. As the experimental data used by the identification methods are nodal displacements, the displacement residual (Equation (16)) is naturally exploited. This residual is defined locally as the difference between two displacements. It carries meaningful information about potential problems in the identification procedure. For a simple overview, the global displacement residual χ is defined as the norm of the nodal displacement residual

$$\chi^2(\underline{\mathbf{p}}) = \frac{1}{n_\varphi} \|\underline{\mathbf{r}}_{\mathbf{u}}(\underline{\mathbf{p}})\|^2_{\mathbb{C}_u^{-1}}. \tag{36}$$

The squared norm is divided by n_φ, the number of displacement degrees of freedom for the sake of interpretation. In the case of a perfect identification (i.e., if the displacement residual is only due to displacement uncertainties), χ statistically converges to 1 (with its variance equal to $2/n_\varphi$). If χ is close to 1, it is likely that the residuals between measured and simulated displacements are only due to the displacement uncertainties. If χ is significantly greater than 1, some displacements are not explained by the uncertainties but are due to model error.

4.2. Synthetic experiments

For comprehensive analyses, the EGM reconditioning is first investigated for synthetic experiments, where the reference value of the Poisson's ratio denoted ν_{ref} is a priori chosen. A series of synthetic experiments are conducted to run identifications with and without measurement uncertainties, and to examine the influence

of the values of the Poisson's ratio and boundary conditions. The synthetic experiments use the same geometry as the real test.

4.2.1. Synthetic experiment with perfect measurements

The identification methods are first investigated with fields designed as perfect measurements. They consist of 1,000 displacement fields, which are solutions to elastic problems. The boundary conditions of the simulations are measured displacements prescribed on the non-free boundary nodes for image I_1, i.e., at the first loading step. The material parameters are the Young's modulus, but its value does not affect the displacement field as only Dirichlet boundary conditions are used, and the Poisson's ratio ν with values in the range $[-1, 0.5]$. The elastic problems to design the simulated displacement fields, as well as the identification procedures, use the same FE mesh.

The error between the reference Poisson's ratio ν_{ref} assumed for designing the simulated displacement fields and the identified Poisson's ratio for the various parameterizations and methods is plotted in Figure 4. For the two parameterizations and all the identification methods, the errors are very small. They are mainly attributed to numerical imprecision. Therefore, all identification procedures are proficient. FEMU sometimes gives higher errors than EGM, REGM, and SREGM. The behavior of the optimization algorithm explains these FEMU errors. They depend on the initial guess and on the stopping criterion. For the interpolation parameterization, few outliers are caused by the stopping criterion, which is activated before the optimality criterion.

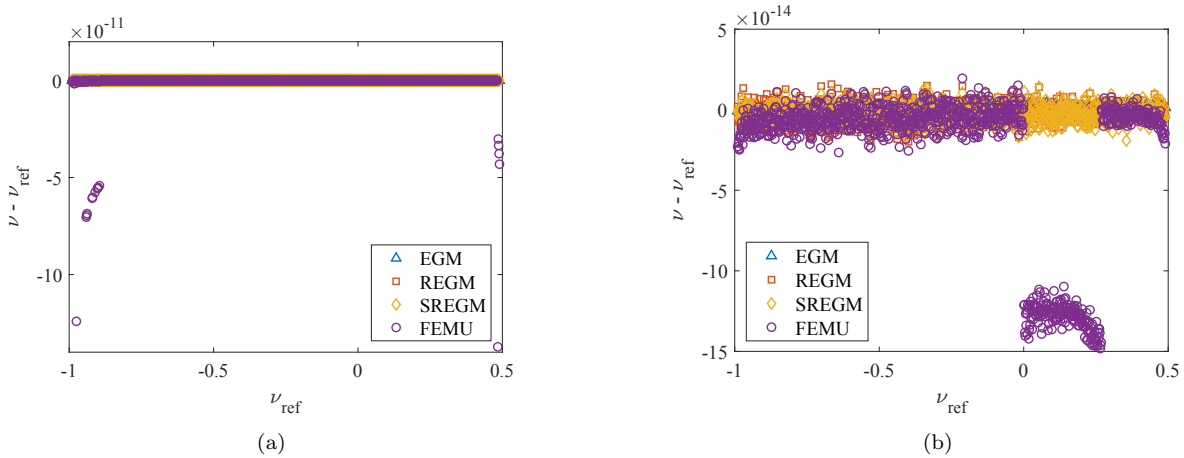

Figure 4: Identification error for perfect synthetic measurements with the interpolation (a) and the spectral (b) parameterizations.

Higher errors are observed for FEMU for the subset $\nu_{ref} \in [0,\ 0.25]$ for the spectral parameterization. They are due to the end of the optimization procedure. The stopping criterion is reduced by a factor of 100 at each iteration. The process stops in the subset with high errors just after the criterion threshold. In contrast, for the other parameters, the second to last step is just before the criterion threshold. The last step leads to a residual less than the stopping criterion (Figure 5).

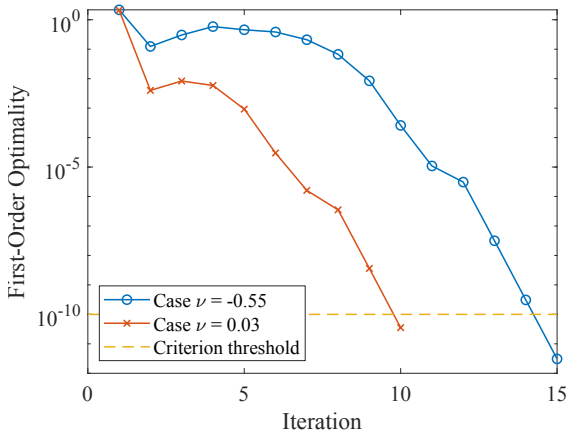

Figure 5: Evolution of the First-Order Optimality measure [56] (i.e., criterion based on the cost-function and constraint gradients [44]) for two reference Poisson's ratios with FEMU.

4.2.2. *Synthetic experiments with measurement uncertainties and various Poisson's ratios*

The synthetic experiment consists of $1,000$ displacement fields generated with the same geometry and mesh as before. The Young's modulus is again chosen as unitary. The reference values of the Poisson's ratio are selected in the range $[-1, 0.5]$. The boundary conditions employed for the simulation are the displacements measured for image I_1, which corresponds to the smallest signal-to-noise ratio, and image I_6, which is associated with a higher displacement level. Measurement uncertainties are generated from a centered Gaussian distribution using the DIC covariance matrix $\mathbb{C}_u$.

The error between the reference values ν_{ref} and the Poisson's ratios identified by various methods is shown in Figure 6 for the interpolation and spectral parameterizations (Appendix B). All the points for the EGM error are not visible as they vary linearly according to the reference value for both parameterizations. The EGM gives biased results with a direction depending on the parameterization. This bias saturates the inequality constraints, making ν_{EGM} constant, and therefore, the error is linear with respect to ν_{ref}. The interpolation parameterization always gives $\nu = -1$, whereas the spectral parameterization always yields $\nu = 0.5$. This bias is related to the attraction to the solution $\underline{\mathbf{p}} = \underline{\mathbf{0}}$ discussed with Equation (5) in Section 2.2.

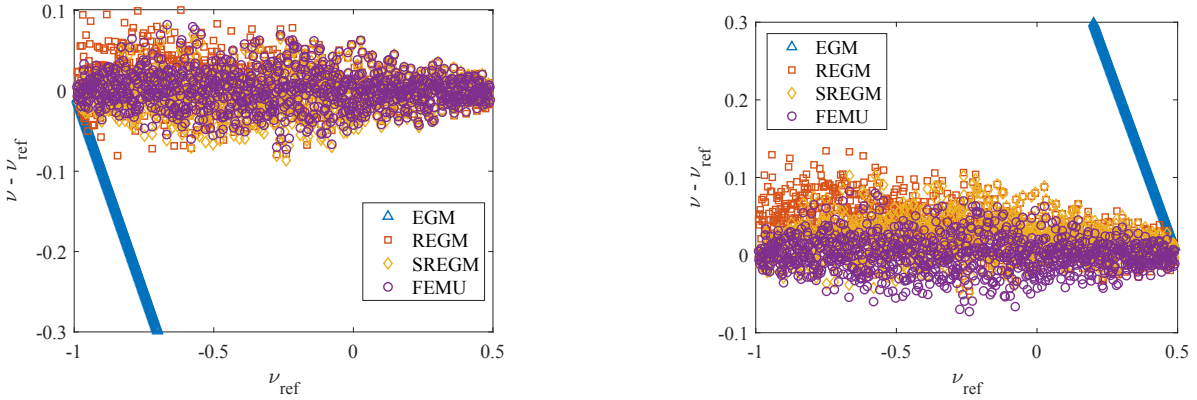

Figure 6: Identification error for synthetic experiments including measurement uncertainties with the interpolation parameterization (a) and the spectral decomposition (b) using boundary conditions of image I_1 (i.e., $F = 1$ kN).

The only mathematical difference between the two optimization problems lies in the equality constraint, which restricts the acceptable parametric space differently. Without these constraints, both parameteriza-

tions represent any plane stress and isotropic Hooke's tensor and are thus equivalent. Performing identifications with any parameterization with the same equality constraint in the parametric space leads to the same bias. Therefore, the bias depends on the equality constraint. REGM and SREGM do not suffer as significantly as the EGM from this bias, but it is still observable for the spectral parameterization. FEMU does not suffer from bias, its error is constant for any reference value of the Poisson's ratio.

The presence of bias is linked to the cost function on which the identification method is based. Analytically, the analysis of FEMU and EGM (formulated as particular cases of VFM) confirms that bias is expected in EGM in the presence of uncertainties on measured displacement [5]. A similar numerical analysis to the one carried out herein has been conducted for the problem of identifying properties of elastomechanical systems [57]. The "input residual method," which minimizes the equilibrium equations using measured displacements (i.e., EGM herein) shows a bias compared to the "output residual method", which simulates displacements and compares them to measurements (i.e., FEMU). In addition, appropriate covariance weighting of the input residual method greatly reduces the bias and the variance [58]. This improvement is similar to the effect of reconditioning in REGM, which is constructed using covariance weighting (Section 3.2).

The results for another synthetic experiment using Dirichlet boundary conditions constructed from the displacement field measured for image I_6 are shown in Figure 7. The EGM bias depends on the material parameter for reference values of ν far from the maximum and minimum acceptable values (above 0.5 for the interpolation parameterization and under 0.2 for the spectral decomposition). When the reference Poisson's ratio is close to the limit values, the bias pushes the identification toward the limit. The identified values are constrained, which leads to a linear dependency of the error with respect to the reference values. The high uncertainty sensitivity may explain why the optimization for the EGM prefers a solution close to zero rather than the true solution. Excluding the case $\underline{\mathbf{p}} = \underline{\mathbf{0}}$, the residuals cannot vanish because of measurement uncertainties even if the residual is calculated with the exact parameters $\underline{\mathbf{p}}_{ref}$. It is consistent with the fact that such a bias does not occur with displacements with no uncertainties (Section 4.2.1). This analysis is also reinforced by the observation that increasing the signal-to-noise ratio reduces the bias, comparing

Figures 6 and 7. In addition to the bias, EGM results exhibit higher uncertainties than the other methods, which is consistent with a higher spectral sensitivity [3].

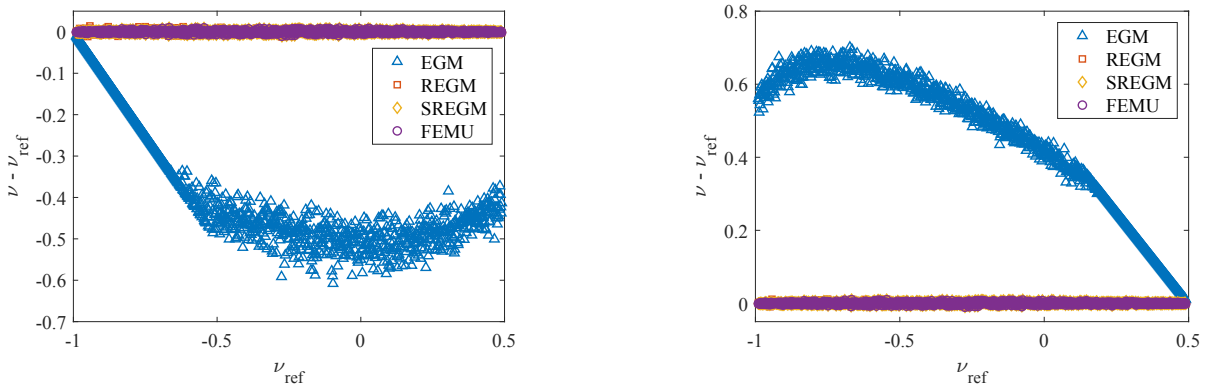

Figure 7: Identification error for synthetic experiments including measurement uncertainty with the interpolation parameterization (a) and the spectral decomposition (b) using boundary conditions of image I_6 ($F = 6$ kN).

To extend the analysis quantitatively, Table 1 displays the mean and standard deviation of the error for both synthetic experiments for EGM, REGM (with different norms) and FEMU. With no bias, the mean error should converge to zero when the number of simulations increases. The standard deviations of the REGM and FEMU errors give a scale to compare the identification error to the uncertainty. This analysis may be improved as the errors are calculated using different Poisson's ratios. Thus, as seen before, the standard deviation (and the bias) varies with the parameter of interest. However, taking into account these changes allows for the same analysis. Thus, for the sake of simplicity, only this simple version is presented. The REGM bias is significantly smaller than the EGM bias for both parameterizations due to reconditioning, even with the Euclidean norm on the vector $\underline{\mathbf{u}}_{REGM}$, which does not consider the influence of element size.

Using the $\mathbb{M}$-norm (Equation (33)) reduces the bias and yields similar results as weighting by the covariance matrix, which is linked to the number of pixels available for each degree of freedom. Therefore, as the $\mathbb{M}$ norm accounts for the element size, it is a rough approximation of the covariance matrix. The true covariance matrix also depends on the image gradient. Thus, this approximation would be weaker for images with bad speckle patterns [45]. REGM with the norm based on the covariance gives mean relative

errors at least one order of magnitude higher than the FEMU errors. The FEMU mean error is negligible compared to the standard deviation, whereas the REGM mean errors are not negligible. The bias of the EGM has been reduced when using reconditioning, but the REGM bias still has not vanished. FEMU gives the same results for the two parameterizations. Therefore, FEMU is not affected by bias, which would lead to different results for the two parameterizations. This hypothesis is consistent with the explanation that bias is caused by the attraction to $\underline{\mathbf{p}} = \underline{\mathbf{0}}$, which does not exist in FEMU.

Table 1: Mean and standard deviation of the error using REGM and FEMU with various norms and parameterizations for synthetic experiments based on images I_1 and I_6, including measurement uncertainties.

	Mean					**Standard deviation**	
	EGM	REGM			FEMU	REGM	FEMU
Norm	$\mathbb{M}$	$\mathbb{1}$	$\mathbb{M}$	$\mathbb{C}_u^{-1}$	$\mathbb{C}_u^{-1}$	$\mathbb{C}_u^{-1}$	$\mathbb{C}_u^{-1}$
$\underline{\mathbf{p}}$	$(c_0, c_{0.5})$						
I_1	-0.75	1.10×10^{-2}	7.44×10^{-3}	7.35×10^{-3}	9.1×10^{-4}	2.8×10^{-2}	2.3×10^{-2}
I_6	-0.40	2.80×10^{-4}	1.82×10^{-4}	2.42×10^{-4}	6.7×10^{-5}	3.8×10^{-3}	3.1×10^{-3}
$\underline{\mathbf{p}}$	(c_1, c_2)						
I_1	0.75	7.50×10^{-2}	3.92×10^{-3}	3.40×10^{-3}	9.1×10^{-4}	3.0×10^{-3}	2.3×10^{-2}
I_6	0.46	1.98×10^{-3}	1.04×10^{-3}	1.01×10^{-3}	6.7×10^{-5}	3.6×10^{-3}	3.1×10^{-3}

Pearson's correlation coefficients between identification errors obtained by REGM, SREGM, and FEMU are gathered in Table 2 for both parameterizations. The errors between different methods are correlated, meaning that the effect of measurement uncertainties is similar for all approaches. This trend was expected since REGM and SREGM formulations are approximations of FEMU. For both parameterizations, the SREGM errors are more correlated to FEMU errors than to REGM errors, proving that SREGM reduces the effect of the approximation compared to the REGM formulation.

Table 2: Correlations between the identification errors (in ν) for results simulated with image I_1.

	Parameterization	
Compared methods	Interpolation	Spectral
REGM - SREGM	0.66	0.69
REGM - FEMU	0.69	0.76
SREGM - FEMU	**0.98**	**0.94**

4.2.3. Synthetic experiments with model error

The experimental data indicate that damage occurred in the sample (Figures 3(b) and 18(b)). Previous works have identified damage fields [4] and damage law [10, 43] for this experiment. In this section, damage is not represented explicitly but is considered as a model error with respect to a perfectly elastic model. The Poisson's ratio is identified from simulated displacement fields with experimentally measured boundary conditions and damage field to analyze the effect of model errors for the different methods.

The synthetic data consists of $1,100$ displacement fields generated on the same mesh as previously. The generation of the simulated nodal displacements is performed in three steps. First, the set of 11 experimentally measured nodal displacements $\underline{\mathbf{u}}_k$ is enriched by linear (temporal) interpolation into a new set $\underline{\mathbf{u}}_i^{(\text{interp})}$. Between $\underline{\mathbf{u}}_0 = \underline{\mathbf{0}}$ and $\underline{\mathbf{u}}_1$, and then between two consecutive displacement fields $\underline{\mathbf{u}}_k$ associated with image I_k and $\underline{\mathbf{u}}_{k+1}$, 100 fields are created by linear interpolation (uniformly distributed)

$$\begin{cases} \underline{\mathbf{u}}_i^{(\text{interp})} = \frac{i-1}{100}\underline{\mathbf{u}}_1 & i \in [1, 100] \\ \underline{\mathbf{u}}_i^{(\text{interp})} = \frac{i-100(k-1)}{100}\underline{\mathbf{u}}_k + \frac{100k-i}{100}\underline{\mathbf{u}}_{k-1} & i \in [100(k-1)+1, 100\ k],\ k \in [2, 11]. \end{cases} \tag{37}$$

Then, a damage field is calculated for every field of the augmented set of measured displacements. An element is considered damaged (i.e., $D = 0.99$) if the major principal strain is greater than a threshold strain and undamaged ($D = 0$) otherwise. The threshold strain is chosen to be 0.02, which is the level for which macroscopic damage appears for this material [49]. Figure 8 shows the damage field for the simulations corresponding to images I_9, I_{10} and I_{11}.

Last, for each displacement field of the enriched data set, an elastic simulation is performed with the measured boundary conditions assuming an isotropic material with a Poisson's ratio $\nu_{ref} = 0.31$ and the effective elastic property associated with the calculated damage field. The displacement fields obtained from these simulations are the synthetic data employed to test the identification methods. No uncertainties are added to the simulated displacement fields so that the main source of error is due to damage when $\nu = \nu_{ref}$.

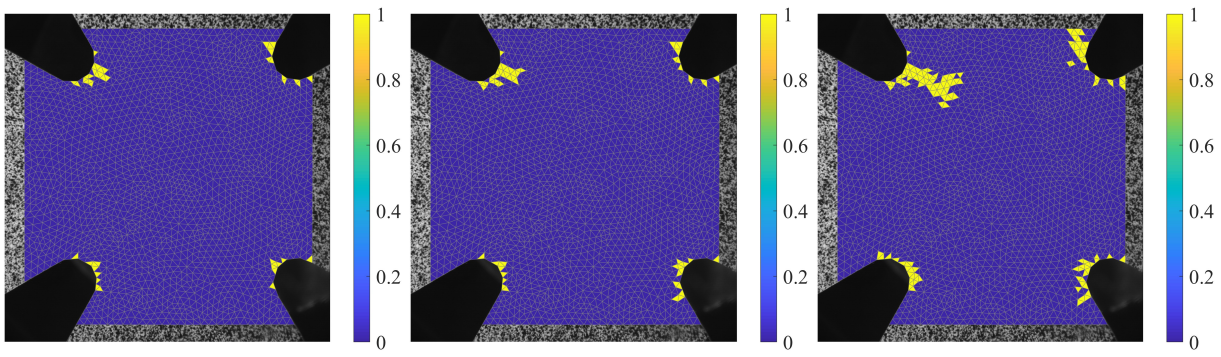

Figure 8: Damage fields used for the synthetic experiments corresponding to image I_9 (a), I_{10} (b) and I_{11} (c).

Figure 9 shows the identified values of the Poisson's ratio ν with the different methods. When there is no damage (i.e., up to image I_5), all identification methods give the reference value with no error. When damage occurs, bias affects EGM, and its results approach -1. The other three methods behave similarly. First, the value of ν increases slightly as damage increases, and between images I_{10} and I_{11}, the value becomes significantly underestimated. When the model error leads the identification methods to overestimate ν, SREGM results fall between REGM and FEMU, as expected. When ν is underestimated, SREGM results do not lie between FEMU and REGM, as the link between REGM (and therefore SREGM) and FEMU only holds if the model error is small.

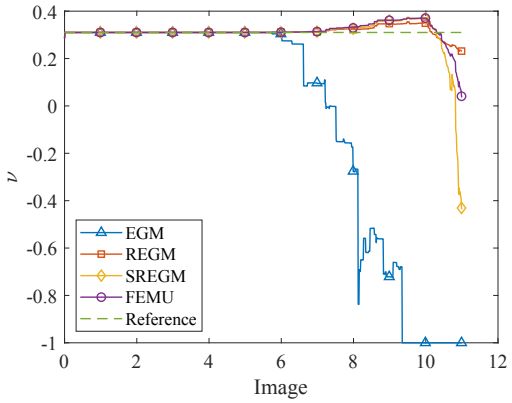

Figure 9: Poisson's ratio identified by the different methods ($\nu_{ref} = 0.31$) for the synthetic experiment with a model error.

4.3. Real experiment

The various identification methods are now investigated for the displacements measured from the series of images captured during the real experiment.

4.3.1. Identification over the whole image series

The identification for the real experiment is performed using the same methods as for the synthetic experiments on the displacement fields corresponding to images I_1 to I_{11}. Figure 10(a) shows the Poisson's ratio identified for each image independently. The EGM bias is present in the results as the Poisson's ratio is pushed against its minimum value before image I_3 and after image I_8. In between, it increases toward the results of the other methods but never reaches comparable values. These results are poor, as the residuals will later confirm. Biases may result from a low signal-to-noise ratio (SNR) and/or model error. The results corresponding to images I_6 and I_7 are the least affected by EGM bias, which is likely due to their highest SNR and lowest model error. The influence of the parameterization on the EGM bias is also illustrated in Appendix C from the results using the spectral parameterization.

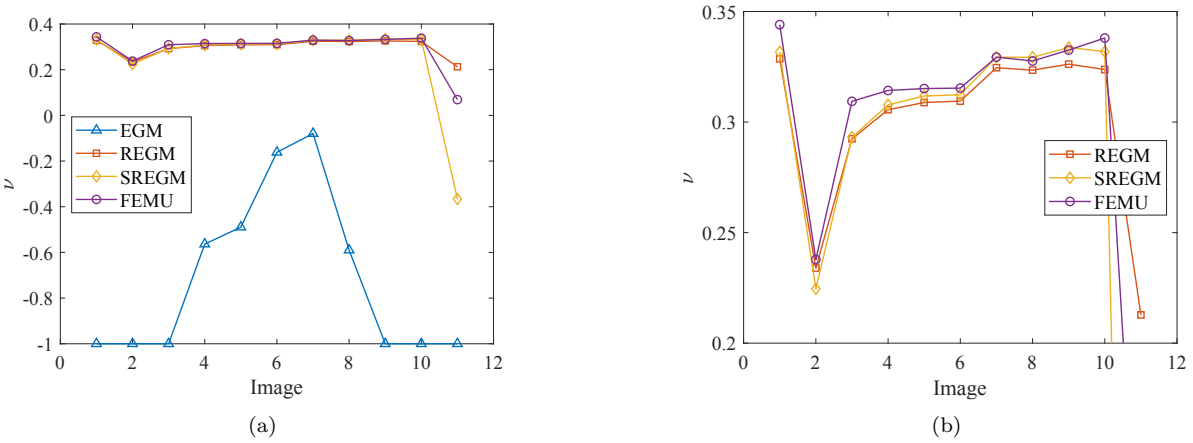

Figure 10: Identification results based on measured displacement fields using the interpolation parameterization. All results (a) and focus on a limited range (b).

REGM, SREGM and FEMU results are consistent with each other until the last image, where they differ because the crack is large and thus model errors occur (Figure 10(b)). Some variations occur in the first two images, where the SNR is low. For images I_3 to I_6, the methods converge with similar trends toward

the value of 0.31, which was also found in previous studies [33]. From images I_6 to I_7, the Poisson's ratio increases probably because of damage initiation. This increase is consistent with a strain threshold of 2% [49], which is exceeded after image I_6. For images I_7 to I_{10}, the REGM results oscillate and those of SREGM and FEMU slightly increase. The outputs of all methods drop for the last image, due to macrocrack propagation. Its formulation and the synthetic experiments showed that the SREGM behaves as an intermediate route between REGM and FEMU when no model error is present. This trend is confirmed for the usable range of images I_3 to I_6.

The analysis of the displacement residuals (Figure 11(a)) confirms that the EGM results are poor compared to all other methods. Regarding the other methods, the displacement residuals are very similar (i.e., a relative difference less than 0.2%). The gradual increase of the residuals with applied force indicates that the model used for identification purposes (i.e., isotropic, plane stress elasticity) is insufficient to describe the measured displacements even before damage occurs. The initiation and propagation of the main crack explain the high residuals in the last image.

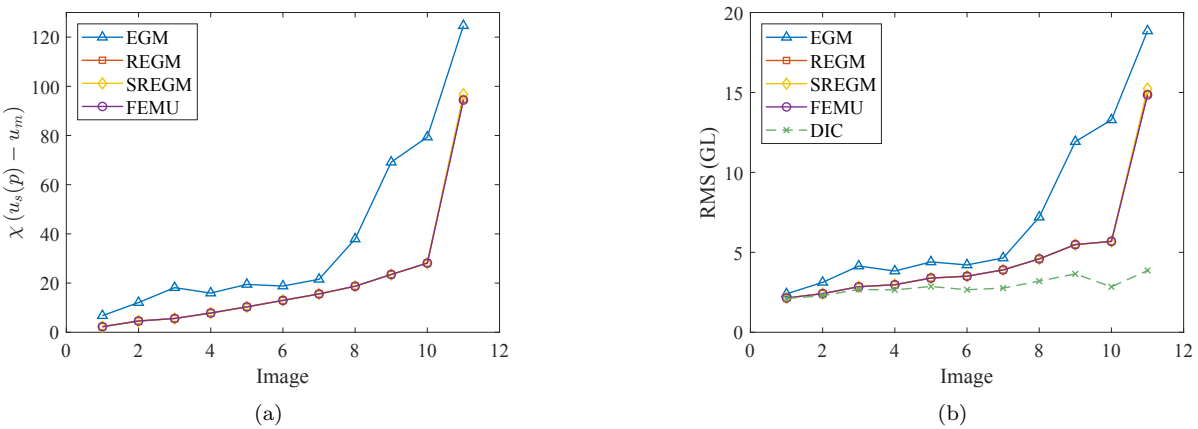

Figure 11: Errors in terms of displacements (a) and gray level (b) residuals for each image depending on the identification method using the interpolation parameterization

Figure 11(b) displays the gray level residuals (Appendix D) for each identification result and raw DIC. They exhibit similar trends as the displacement residuals. The DIC residuals slightly increase after image I_8, which may indicate that the FE mesh is too coarse to capture the displacements near the cracks.

Figure 12 shows the computation time for each method and each image. All calculations were run

on a computer with two Intel(R) Xeon(R) CPUs E5-2630 v4 (Broadwell) at 2.20 GHz. The run time only includes the construction and calculation associated with the optimization problems (i.e., operations performed for each displacement field). The total computation time includes preparation (i.e., 1.5 s), which does not depend on the number of identifications, and construction of the surrogate model, which only slightly depends on the number of iterations. As expected, EGM and REGM are much faster than FEMU and SREGM. SREGM is faster than FEMU per iteration, but taking into account the construction of the surrogate model, the two methods have similar computation times. This observation cannot be generalized, as the benefit of the surrogate highly depends on the number of analyzed displacement fields.

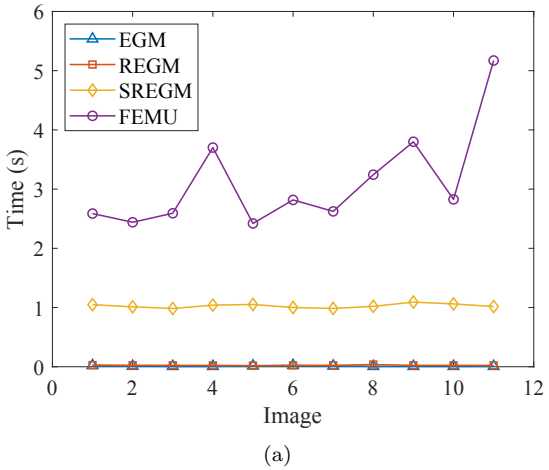

(a)

Figure 12: Computation time for each image depending on the identification method.

4.3.2. Identification excluding the crack

As seen before, the crack (and damage) on the last loading step causes the failure of all identification methods. An easy improvement is removing the part of the sample where the crack propagates so that damage mechanisms may not perturb the identification methods. The nodes of the elements where the crack appears are defined as Dirichlet nodes (where the equilibrium is not calculated and minimized). Figure 13 shows the mesh with the mask applied to the nodes excluding the crack.

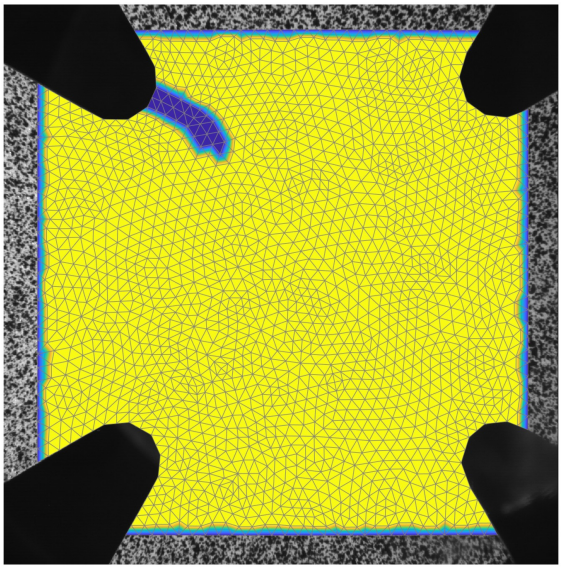

Figure 13: FE mesh used for identifications excluding the crack. The color represents the mask used for evaluating the equilibrium residual: yellow indicates points where the equilibrium can be evaluated and is minimized, and blue indicates points where the equilibrium is unknown and ignored.

Figure 14 shows the identification results obtained with the mesh excluding (Figure 13) or including the cracked zone. Between images I_3 and I_{10}, the results are consistent even though the two identification domains differ. Removing the crack cancels out most of the sharp drop occurring for image I_{11} in the results, though not entirely presumably because other regions are also damaged (Figures 3(b) and 8). In both cases, SREGM values lie between REGM and FEMU levels for images I_3 to I_7. EGM results, which are not visible in Figure 14, are still biased and mainly similar to the ones obtained with the mesh including the crack. The maximum Poisson's ratio identified by EGM is $\nu_{EGM} = -0.12$ for image I_7.

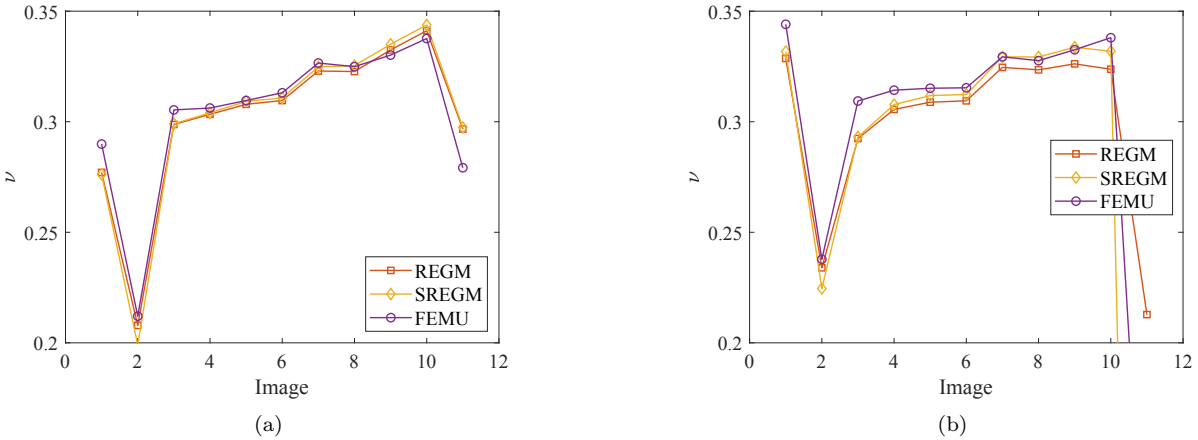

Figure 14: Identification results based on measured displacement fields for the mesh without (a) and with (b) the crack using the interpolation parameterization.

Figure 15 displays the gray level residuals for both meshes. Excluding the crack reduces the residuals of all methods for images after I_7, particularly for image I_{11}. The residuals with EGM results are greatly reduced but are still above the other three methods. REGM, SREGM and FEMU residuals decrease after image I_6 confirming that the model error has been reduced. The residuals still increase with loading (with values greater than the raw DIC residuals), showing that damage may also have occurred in other places, or model errors related to elastic isotropy [50], or both.

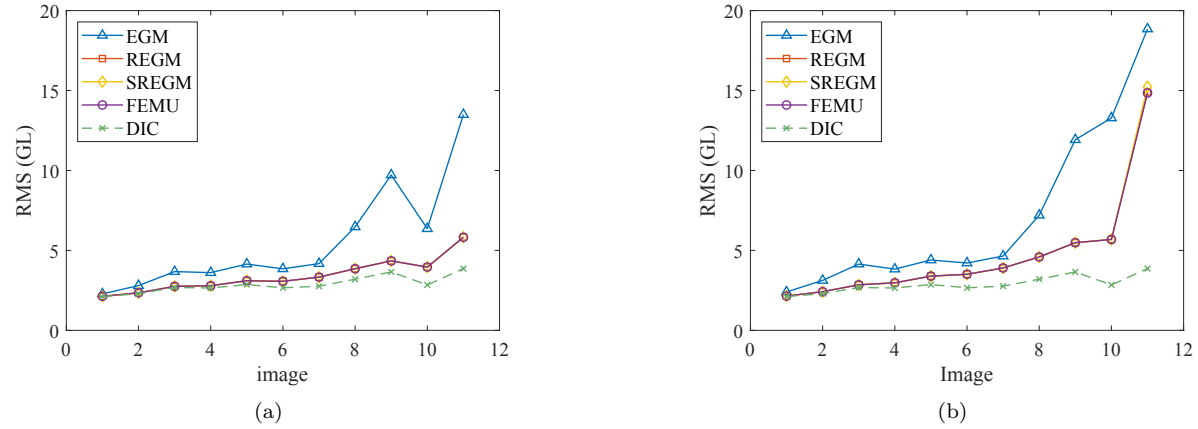

Figure 15: Errors in terms of gray level residuals for the mesh without (a) and with (b) the crack for each image depending on the identification method using the interpolation parameterization.

5. Conclusion

This work presented different variants for identifying elastic parameters with the equilibrium gap method (EGM), which minimizes norms of local equilibrium residuals. The EGM has the advantage of being direct and computationally inexpensive compared to other identification methods, which generally are iterative. However, it is limited to the use of full-field measurement, has a high sensitivity to measurement uncertainties, and may yield biased results. Even though not discussed herein, it is worth noting that the EGM cost function was very useful for constructing a mechanical filter in regularized DIC/DVC [11, 12, 14, 15].

When the EGM cost function does not account for resultant forces nor body forces, it is homogeneous of degree two with respect to the Young's modulus (or similarly, with respect to Lamé's moduli). Thus, without force measurements, a material with vanishing stiffness is a solution to the optimization problem. More generally, reducing the stiffness reduces the EGM cost function independently of true material parameters, which explains the bias that was observed when calibrating the Poisson's ratio with the original (EGM) cost function. The Reconditioned EGM (REGM) retains its predecessor advantages while lowering its uncertainty sensitivity and significantly reducing bias.

Uncertainties in the measured displacements were shown to be one cause of biased results. The variability of EGM results is generally higher than those of the other investigated procedures. This work investigated different reconditioning routes to mitigate such drawbacks. Reconditioning was initially introduced as a way of mending high sensitivities to measurement uncertainties. It was proven herein that it could also be seen as an approximation of a covariance weighting of the least-squares EGM cost function. The bias was reduced with the REGM because the reconditioned formulation accounted for measurement uncertainties; thus the signal is more easily distinguished from noise. The EGM was also shown to be sensitive to model error; the REGM was on par with FEMU in that context.

This work illustrated the fact that the EGM may not be the best path for identification purposes. Conversely, REGM yielded accurate results similar to FEMU with a fraction of the computational cost. In favorable conditions, when there is no model error and a good signal-to-noise ratio, REGM was shown to be a close approximation of FEMU. A finite element simulation using the identified parameters easily indicates

whether the REGM-FEMU approximation holds. Thus, REGM, used in conjunction with a verification of the results, is an efficient identification route, for instance, for cases when the computational cost is an issue. It is worth noting that the reconditioning may include the unknown parameters. This observation led to the introduction of the Sequentially Reconditioned EGM. It generally improved the FEMU approximation but increased the computational cost as well.

Statements and Declarations

The authors declare that they have no conflict of interest.

References

[1] S. Avril, M. Bonnet, A.-S. Bretelle, M. Grédiac, F. Hild, P. Ienny, F. Latourte, D. Lemosse, S. Pagano, E. Pagnacco, and F. Pierron. Overview of identification methods of mechanical parameters based on full-field measurements. Experimental Mechanics, 48(4):381–402, 2008.

[2] M. Grediac and F. Hild, editors. Full-Field Measurements and Identification in Solid Mechanics. John Wiley & Sons, Ltd, 2012.

[3] S. Roux and F. Hild. Optimal procedure for the identification of constitutive parameters from experimentally measured displacement fields. International Journal of Solids and Structures, 184:14–23, 2020.

[4] D. Claire, F. Hild, and S. Roux. A finite element formulation to identify damage fields: the equilibrium gap method. International Journal for Numerical Methods in Engineering, 61(2):189–208, 2004.

[5] S. Avril and F. Pierron. General framework for the identification of constitutive parameters from full-field measurements in linear elasticity. International Journal of Solids and Structures, 44(14-15):4978–5002, 2007.

[6] E. Florentin and G. Lubineau. Identification of the parameters of an elastic material model using the constitutive equation gap method. Computational Mechanics, 46(4):521–531, 2010.

[7] G. Lubineau and E. Florentin. The global equilibrium method and its hybrid implementation for identifying heterogeneous elastic material parameters. Computers & Structures, 89(7):656–667, 2011.

[8] A. Moussawi, G. Lubineau, E. Florentin, and B. Blaysat. The constitutive compatibility method for identification of material parameters based on full-field measurements. Computer Methods in Applied Mechanics and Engineering, 265:1–14, 2013.

[9] J. M. P. Martins, A. Andrade-Campos, and S. Thuillier. Comparison of inverse identification strategies for constitutive mechanical models using full-field measurements. International Journal of Mechanical Sciences, 145:330–345, 2018.

[10] S. Roux and F. Hild. Digital image mechanical identification (DIMI). Experimental Mechanics, 48(4):495–508, 2008.

[11] J. Réthoré, S. Roux, and F. Hild. An extended and integrated digital image correlation technique applied to the analysis of fractured samples. European Journal of Computational Mechanics, 18(3-4):285–306, 2009. Publisher: Taylor & Francis.

[12] Z. Tomicevic, F. Hild, and S. Roux. Mechanics-Aided Digital Image Correlation. Journal of Strain Analysis for Engineering Design, 48:330–343, 2013. Publisher: SAGE Publications.

[13] H. Leclerc, J.-N. Périé, S. Roux, and F. Hild. Voxel-Scale Digital Volume Correlation. Experimental Mechanics, 51(4):479–490, 2011.

[14] T. Taillandier-Thomas, S. Roux, T. F. Morgeneyer, and F. Hild. Localized strain field measurement on laminography data with mechanical regularization. Nuclear Instruments and Methods in Physics Research Section B: Beam Interactions with Materials and Atoms, 324:70–79, 2014.

[15] A. Mendoza, J. Neggers, F. Hild, and S. Roux. Complete Mechanical Regularization Applied to Digital Image and Volume Correlation. Computer Methods in Applied Mechanics and Engineering, 355:27–43, 2019. Publisher: Elsevier.

[16] H. Leclerc, J. Périé, F. Hild, and S. Roux. Digital volume correlation: What are the limits to the spatial resolution? Mechanics & Industry, 13:361–371, 2012.

[17] M. Grédiac. Principe des travaux virtuels et identification. Comptes Rendus de l'Académie des Sciences, 309, 1989.

[18] F. Pierron and M. Grédiac. The Virtual Fields Method. Springer New York, 2012.

[19] M. Grédiac, F. Pierron, S. Avril, E. Toussaint, and M. Rossi. Virtual Fields Method, The, chapter 11, pages 301–330. John Wiley & Sons, Ltd, 2013.

[20] K. Kavangh and R. Clough. Finite element applications in the characterization of elastic solids. International Journal of Solids and Structures, 7(1):11–23, 1971.

[21] J. Collins, G. Hart, T. Hasselman, and B. Kennedy. Statistical identification of structures. AIAA J., 12(2):185–190, 1974.

[22] E. Pagnacco, A.-S. Caro-Bretelle, and P. Ienny. Parameter Identification from Mechanical Field Measurements using Finite Element Model Updating Strategies, chapter 9, pages 247–274. John Wiley & Sons, Ltd, 2013.

[23] P. Ladevèze, M. Reynier, and N. M. M. Maia. Error localization for updating FE models using frequency response function. Proceedings of SPIE, 1994.

[24] S. Pagano and M. Bonnet. Constitutive Equation Gap, chapter 10, pages 275–300. John Wiley & Sons, Ltd, 2013.

[25] G. Geymonat, F. Hild, and S. Pagano. Identification of elastic parameters by displacement field measurement. Comptes Rendus Mécanique, 330(6):403–408, 2002.

[26] F. Latourte, A. Chrysochoos, S. Pagano, and B. Wattrisse. Elastoplastic Behavior Identification for Heterogeneous Loadings and Materials. Experimental Mechanics, 48(4):435–449, 2008.

[27] O. Allix, P. Feissel, and H. Nguyen. Identification strategy in the presence of corrupted measurements. Engineering Computations, 22(5):487–504, 2005.

[28] S. Calloch, D. Dureisseix, and F. Hild. Identification de modèles de comportement de matériaux solides : utilisation

d'essais et de calculs. Technologies et Formations, 100:36, 2002.

[29] M. Ben Azzouna, P. Feissel, and P. Villon. Robust identification of elastic properties using the Modified Constitutive Relation Error. Computer Methods in Applied Mechanics and Engineering, 295:196–218, 2015.

[30] S. Huang, P. Feissel, and P. Villon. Modified constitutive relation error: An identification framework dealing with the reliability of information. Computer Methods in Applied Mechanics and Engineering, 311:1–17, 2016.

[31] H. N. Nguyen, L. Chamoin, and C. Ha Minh. mCRE-based parameter identification from full-field measurements: Consistent framework, integrated version, and extension to nonlinear material behaviors. Computer Methods in Applied Mechanics and Engineering, 400:115461, 2022.

[32] F. Hild and S. Roux. Digital image correlation: from displacement measurement to identification of elastic properties - a review. Strain, 42(2):69–80, 2006.

[33] H. Leclerc, J.-N. Périé, S. Roux, and F. Hild. Integrated digital image correlation for the identification of mechanical properties. In W. Philips and A. Gagalowicz, editors, Computer Vision/Computer Graphics CollaborationTechniques, volume 5496, pages 161–171. Springer Berlin Heidelberg, 2009. Series Title: Lecture Notes in Computer Science.

[34] D. Lindner, F. Mathieu, F. Hild, O. Allix, C. Ha Minh, and O. Paulien-Camy. On the evaluation of stress triaxiality fields in a notched titanium alloy sample via integrated DIC. J. Appl. Mech., 82(7):071014, 2015.

[35] A. Constantinescu. On the identification of elastic moduli. phdthesis, Ecole Polytechnique X, 1994.

[36] S. Andrieux and A. Ben Abda. The reciprocity gap: a general concept for flaws identification problems. Mechanics Research Communications, 20(5):415–420, 1993.

[37] H. D. Bui, A. Constantinescu, and H. Maigre. The reciprocity gap functional for identifying defects and cracks. In Z. Mróz and G. E. Stavroulakis, editors, Parameter Identification of Materials and Structures, CISM International Centre for Mechanical Sciences, pages 17–54. Springer, 2005.

[38] J. Périé, H. Leclerc, S. Roux, and F. Hild. Digital image correlation and biaxial test on composite material for anisotropic damage law identification. International Journal of Solids and Structures, 46:2388–2396, 2009.

[39] F. Amiot, J.-N. Périé, and S. Roux. Equilibrium Gap Method, chapter 12, pages 331–362. John Wiley & Sons, Ltd, 2013.

[40] M. Sutton. Computer vision-based, noncontacting deformation measurements in mechanics: A generational transformation. Applied Mechanics Reviews, 65(AMR-13-1009):050802, 2013.

[41] P. E. Barbone, C. E. Rivas, I. Harari, U. Albocher, A. A. Oberai, and Y. Zhang. Adjoint-weighted variational formulation for the direct solution of inverse problems of general linear elasticity with full interior data. International Journal for Numerical Methods in Engineering, 81(13):1713–1736, 2010.

[42] G. Bal, C. Bellis, S. Imperiale, and F. Monard. Reconstruction of constitutive parameters in isotropic linear elasticity from noisy full-field measurements. Inverse Problems, 30(12):125004, 2014. Publisher: IOP Publishing.

[43] F. Hild, J.-N. Périé, and S. Roux. Evaluating Damage with Digital Image Correlation: C. Applications to Composite Materials. In G. Z. Voyiadjis, editor, Handbook of Damage Mechanics, pages 1301–1322. Springer New York, New York,

NY, 2015.

[44] J. Nocedal and S. J. Wright. Numerical optimization. Springer series in operations research. Springer, New York, 2nd ed edition, 2006. OCLC: ocm68629100.

[45] F. Hild and S. Roux. Digital image correlation. In Optical methods for solid mechanics. A full-field approach, pages 183–228. P. Rastogi and E. Hack, eds. Wiley-VCH, Weinheim (Germany), 2012.

[46] P. Pilvin. Identification des paramètres de modèles de comportement,. In Proc. Mecamat, pages 155–164, 1988.

[47] R. Gras, H. Leclerc, F. Hild, S. Roux, and J. Schneider. Identification of a set of macroscopic elastic parameters in a 3D woven composite: Uncertainty analysis and regularization. International Journal of Solids and Structures, page 15, 2013.

[48] C. Brezinski and M. Redivo–Zaglia. The genesis and early developments of Aitken's process, Shanks' transformation, the ε–algorithm, and related fixed point methods. Numerical Algorithms, 80(1):11–133, 2019.

[49] F. Collin, Y. Berthaud, and F. Hild. Visualisation par analyse d'images de la répartition des déformations et de l'amorçage dans un matériau composite. In Y. Berthaud, M. Cottron, F. Morestin, P. Moucheront, and M. Taroni, editors, Photomécanique 98, pages 241–248. GAMAC, 1998.

[50] S. Roux and F. Hild. Comprehensive full-field measurements via Digital Image Correlation. In V. Silberschmidt, editor, Comprehensive Mechanics of Materials. Elsevier, 2024.

[51] J. Lemaitre. A Course on Damage Mechanics. Springer Berlin Heidelberg, Berlin, Heidelberg, 1992.

[52] S. Roux, J. Réthoré, and F. Hild. Digital image correlation and fracture: an advanced technique for estimating stress intensity factors of 2D and 3D cracks. Journal of Physics D: Applied Physics, 42(21):214004, 2009.

[53] J. Tong. Full-field characterisation of crack tip deformation and fatigue crack growth using digital image correlation—a review. Fatigue & Fracture of Engineering Materials & Structures, 41(9):1855–1869, 2018.

[54] MathWorks. Active-set quadprog algorithm, 2023.

[55] MathWorks. Modified fmincon algorithm for constrained least squares, 2023.

[56] MathWorks. First-order optimality measure, 2023.

[57] N. Cottin, H. P. Felgenhauer, and H. G. Natke. On the parameter identification of elastomechanical systems using input and output residuals. Ingenieur-Archiv, 54(5):378–387, 1984.

[58] N. Cottin and H. G. Natke. On the parameter identification of elastomechanical systems using weighted input and modal residuals. Ingenieur-Archiv, 56(2):106–113, 1986.

[59] G. Broggiato. Adaptive image correlation technique for full-field strain measurement. In C. Pappalettere, editor, 12th International Conference on Experimental Mechanics, pages 420–421. McGraw Hill, Lilan (Italy), 2004.

[60] Y. Sun, J. Pang, C. Wong, and F. Su. Finite-element formulation for a digital image correlation method. Applied Optics, 44(34):7357–7363, 2005.

[61] G. Besnard, F. Hild, and S. Roux. "Finite-Element" Displacement Fields Analysis from Digital Images: Application to Portevin–Le Châtelier Bands. Experimental Mechanics, 46(6):789–803, 2006.

A. Covariance weighting for FEMU using measured boundary conditions

This appendix presents the construction of the covariance matrix as the weighting of the FEMU cost function, which takes into account uncertainties associated with the measured displacements used as Dirichlet boundary conditions in the simulations.

The simulated nodal displacements are calculated with the system presented in Section 3.3, which included the weak form of the equilibrium equations and the Dirichlet boundary conditions prescribed via Lagrange multipliers

$$\begin{cases} \mathbb{K}(\underline{\mathbf{p}})\underline{\mathbf{u}}_s(\underline{\mathbf{p}}) + \mathbb{A}^\top \underline{\lambda}_s(\underline{\mathbf{p}}) & = \underline{\mathbf{f}} \\ \mathbb{A}\underline{\mathbf{u}}_s(\underline{\mathbf{p}}) & = \mathbb{A}\underline{\mathbf{u}}_m. \end{cases} \tag{38}$$

In the above system, the degrees of freedom contained in the solution vector $\underline{\mathbf{x}} = [\underline{\mathbf{u}}_s^\top \ \underline{\lambda}_s^\top]^\top$ are the nodal displacements and the Lagrange multipliers are used to prescribe Dirichlet boundary conditions. The right-hand side $\underline{\mathbf{b}} = [\underline{\mathbf{f}}^\top \ (\mathbb{A}\underline{\mathbf{u}}_m)^\top]^\top$ contains the nodal forces and the prescribed displacements. The extractor matrices $\mathbb{E}_u$ and $\mathbb{E}_\lambda$ are defined as

$$\begin{cases} \underline{\mathbf{u}}_s & = \mathbb{E}_u \underline{\mathbf{x}} \\ \underline{\lambda} & = \mathbb{E}_\lambda \underline{\mathbf{x}} \\ \underline{\mathbf{x}} & = \mathbb{E}_u^\top \underline{\mathbf{u}}_s + \mathbb{E}_\lambda^\top \underline{\lambda} \end{cases} \quad \text{and} \quad \begin{cases} \underline{\mathbf{f}} & = \mathbb{E}_u \underline{\mathbf{b}} \\ \mathbb{A}\underline{\mathbf{u}}_m & = \mathbb{E}_\lambda \underline{\mathbf{b}} \\ \underline{\mathbf{b}} & = \mathbb{E}_u^\top \underline{\mathbf{f}} + \mathbb{E}_\lambda^\top \mathbb{A}\underline{\mathbf{u}}_m. \end{cases} \tag{39}$$

Using these matrices, the simulated nodal displacements of system (38) are expressed linearly with respect to $\underline{\mathbf{f}}$ and $\underline{\mathbf{u}}_m$

$$\underline{\mathbf{u}}_s = \mathbb{E}_u \underbrace{\begin{bmatrix} \mathbb{K}(\underline{\mathbf{p}}) & \mathbb{A}^T \\ \mathbb{A} & \mathbb{0} \end{bmatrix}^{-1}}_{\mathbb{K}_{\mathbb{A}}(\underline{\mathbf{p}})} \left(\mathbb{E}_u^\top \underline{\mathbf{f}} + \mathbb{E}_\lambda^\top \mathbb{A}\underline{\mathbf{u}}_m \right). \tag{40}$$

In many cases, $\underline{\mathbf{f}} = \underline{\mathbf{0}}$ because body forces are neglected. To propagate the uncertainties of the measured displacements $\underline{\mathbf{u}}_m$ only, the gradient of the simulated displacement with respect to the measured displacements is necessary. From Equation (40), the gradient $\mathbb{S}_{\underline{\mathbf{u}}_m}(\underline{\mathbf{p}}) = \frac{\partial \underline{\mathbf{u}}_s}{\partial \underline{\mathbf{u}}_m}$ is independent of $\underline{\mathbf{u}}_m$. Thus, for a

fixed parameter set $\underline{\mathbf{p}}$, if the uncertainties on $\underline{\mathbf{u}}_m$ are Gaussian, the uncertainties of $\underline{\mathbf{u}}_s$ are Gaussian as well.

To calculate the covariance matrix of the displacement residual $\underline{\mathbf{u}}_s - \underline{\mathbf{u}}_m$, both nodal displacement vectors are gathered in a single combined vector defined as

$$\begin{bmatrix} \underline{\mathbf{u}}_s \\ \underline{\mathbf{u}}_m \end{bmatrix} = \begin{bmatrix} \mathbb{S}_{\underline{\mathbf{u}}_m}(\underline{\mathbf{p}}) \\ \mathbb{1} \end{bmatrix} \underline{\mathbf{u}}_m. \tag{41}$$

This reformulation allows the covariance matrix of $\underline{\mathbf{u}}_s$ and the correlation between $\underline{\mathbf{u}}_s$ and $\underline{\mathbf{u}}_m$ to be calculated. From the covariance matrix of the measured nodal displacements $\mathbb{C}_u$, the covariance matrix of the combined vector becomes

$$\mathrm{Cov}\left(\begin{bmatrix} \underline{\mathbf{u}}_s(\underline{\mathbf{p}}) \\ \underline{\mathbf{u}}_m \end{bmatrix}\right) = \begin{bmatrix} \mathbb{S}_{\underline{\mathbf{u}}_m}(\underline{\mathbf{p}})\mathbb{C}_u\mathbb{S}^T_{\underline{\mathbf{u}}_m}(\underline{\mathbf{p}}) & \mathbb{S}_{\underline{\mathbf{u}}_m}(\underline{\mathbf{p}})\mathbb{C}_u \\ \mathbb{C}_u\mathbb{S}^T_{\underline{\mathbf{u}}_m}(\underline{\mathbf{p}}) & \mathbb{C}_u \end{bmatrix}. \tag{42}$$

The uncertainties of the simulation and the measurements are correlated. The residual displacement (Equation (16)) is obtained by a linear transformation of the combined vector. Applying this linear transformation to the covariance matrix (42) yields

$$\mathbb{C}_{\underline{\mathbf{r}}_u}(\underline{\mathbf{p}}) = \mathbb{C}_u - \left(\mathbb{S}_{\underline{\mathbf{u}}_m}(\underline{\mathbf{p}})\mathbb{C}_u + \mathbb{C}_u\mathbb{S}^T_{\underline{\mathbf{u}}_m}(\underline{\mathbf{p}})\right) + \mathbb{S}_{\underline{\mathbf{u}}_m}(\underline{\mathbf{p}})\mathbb{C}_u\mathbb{S}^T_{\underline{\mathbf{u}}_m}(\underline{\mathbf{p}}). \tag{43}$$

The negative sign associated with the second term cancels out the covariance of the Dirichlet nodes. One additional step is required to construct the cost function. The displacements associated with Dirichlet boundary nodes are equal to measured displacements

$$\mathbb{A}\underline{\mathbf{r}}_u(\underline{\mathbf{p}}) = \mathbb{A}\underline{\mathbf{u}}_s(\underline{\mathbf{p}}) - \mathbb{A}\underline{\mathbf{u}}_m = \underline{\mathbf{0}}. \tag{44}$$

Thus, the rank of $\mathrm{Cov}(\underline{\mathbf{r}}_u)$ is less than the size of $\underline{\mathbf{r}}_u$. As the inverse covariance matrix is needed to minimize the weighted cost function, the residual only accounts for non-Dirichlet degrees of freedom. Let $\mathbb{B}$ denote the matrix extracting the non-Dirichlet degrees of freedom, the residual vector becomes $\underline{\mathbf{r}}_{u,\mathbb{B}}(\underline{\mathbf{p}}) = \mathbb{B}\underline{\mathbf{r}}_u(\underline{\mathbf{p}})$,

and the corresponding cost function

$$\underline{\mathbf{r}}_{u,\mathbb{B}}(\underline{\mathbf{p}}) \left(\mathbb{B}\ \mathbb{C}_{\underline{\mathbf{r}}_u}(\underline{\mathbf{p}})\ \mathbb{B}^\top\right)^{-1} \underline{\mathbf{r}}_{u,\mathbb{B}}(\underline{\mathbf{p}}). \tag{45}$$

The covariance matrix depends on $\mathbb{S}_{\underline{\mathbf{u}}_d}(\underline{\mathbf{p}})$, which requires a full-matrix inversion. In addition, it depends on the parameter vector $\underline{\mathbf{p}}$. Consequently, minimizing this last cost function requires multiple recalculations of the covariance matrix. In Section 3.2, the same situation appears for the reconditioning matrix of REGM. The computational cost is reduced by assuming $\underline{\mathbf{p}}$ constant for $\mathbb{C}_{\underline{\mathbf{r}}_u}$

$$\mathbb{C}_{\underline{\mathbf{r}}_u}(\underline{\mathbf{p}}) \simeq \mathbb{C}_{\underline{\mathbf{r}}_u}(\underline{\mathbf{p}}_0). \tag{46}$$

This assumption does reduce the computational cost but the residual $\underline{\mathbf{r}}_{u,\mathbb{B}}(\underline{\mathbf{p}})$ is still nonlinear with respect to $\underline{\mathbf{p}}$.

B. Decomposition of Hooke's tensor under plane stress conditions

This appendix presents the construction and analysis of two linear decompositions of Hooke's tensor in plane stress for an isotropic and elastic medium. Let us consider Voigt's notation (i.e., stress and strain tensors are described with the following vectors)

$$\boldsymbol{\sigma} = \left[\sigma_{11}\ \ \sigma_{22}\ \ \sigma_{12}\right]^\top, \quad \boldsymbol{\epsilon} = \left[\epsilon_{11}\ \ \epsilon_{22}\ \ 2\epsilon_{12}\right]^\top. \tag{47}$$

The stiffness matrix in Voigt's notation for an isotropic and elastic material in plane stress reads

$$\mathbf{C}(E,\nu) = \frac{E}{2(1-\nu^2)} \begin{bmatrix} 2 & 2\nu & 0 \\ 2\nu & 2 & 0 \\ 0 & 0 & 1-\nu \end{bmatrix}. \tag{48}$$

B.1. Parameterization based on interpolation

A first parameterization based on a linear interpolation was introduced in Section 4.1.2. The Young's modulus and Poisson's ratio are calculated from $\underline{\mathbf{p}}$ as

$$E = (2\,c_{0.5} + c_0)\,\frac{2\,c_{0.5} + 3c_0}{4\,c_{0.5} + 3\,c_0} \quad \text{and} \quad \nu = \frac{2\,c_{0.5}}{4\,c_{0.5} + 3\,c_0}. \tag{49}$$

The physical meaning behind c_0 and $c_{0.5}$ is not explicit. From the definition domains of E and ν and using Equation (49), the system of linear inequalities that the parameters $c_{0.5}$ and c_0 must satisfy becomes

$$\begin{cases} E \geq 0 \\ \nu \in [-1, 0.5] \end{cases} \Leftrightarrow \begin{cases} 2\,c_{0.5} \geq -c_0 \\ c_0 \geq 0 \end{cases} \Leftrightarrow \underbrace{\begin{bmatrix} 2 & 1 \\ 0 & 1 \end{bmatrix}}_{\mathbb{G}} \underbrace{\begin{bmatrix} c_{0.5} \\ c_0 \end{bmatrix}}_{\underline{\mathbf{p}}} \succcurlyeq \underline{\mathbf{0}}. \tag{50}$$

Due to the nonlinear dependence of E on $c_{0.5}$ and c_0 (Equation (49)), the Young's modulus is not constant when $c_{0.5}$ changes. For the same reasons, the Poisson's ratio ν varies nonlinearly when $c_{0.5}$ ranges from -1 to 1. The equality constraint ($c_{0.5} + c_0 = 1$) is added in the identification procedures to avoid the trivial solution $\underline{\mathbf{0}}$ (Section 4.1.2). This arbitrary choice may have undesirable effects on the results as reported for the synthetic experiments (Section 4.2.2).

B.2. Parameterization based on spectral decomposition

Another parameterization is obtained from the spectral decomposition of Hooke's tensor in Voigt's notation giving $\mathbf{C}(\underline{\mathbf{p}}) = \sum_{i=1}^{3} c_i\ \mathbf{C}_i$ where c_i are the eigenvalues of Hooke's tensor and $\mathbf{C}_i$ the Voigt sitffness matrices of associated eigentensors [8]. This parameterization gives a linear decomposition in the isotropic plane stress case, where only the eigenvalues depend on the parameters. There are three eigenvalues for two parameters. The parameterization is usable because the two eigenvalues c_2 and c_3 are proportional to each other. Therefore, the matrix $[\boldsymbol{C}]$ representing Hooke's tensor in Voigt's notation in two dimensions, with

the eigenvalues replaced by their expressions, reads

$$\boldsymbol{C}(E,\nu) = \underbrace{\frac{1}{2}\frac{E}{1-\nu}}_{c_1}\begin{bmatrix}1 & 1 & 0\\ 1 & 1 & 0\\ 0 & 0 & 0\end{bmatrix} + \underbrace{\frac{1}{2}\frac{E}{1+\nu}}_{c_2}\left(\begin{bmatrix}1 & -1 & 0\\ -1 & 1 & 0\\ 0 & 0 & 0\end{bmatrix} + \begin{bmatrix}0 & 0 & 0\\ 0 & 0 & 0\\ 0 & 0 & 1\end{bmatrix}\right). \tag{51}$$

The two parameters for this decomposition are c_1 and c_2, thus $\underline{\mathbf{p}}$ is defined as $[c_1, c_2]$. Observing the matrices and their eigenvalues, the first matrix is responsible for a hydrostatic state of stress, which is consistent with c_1 being the bulk modulus. The sum of the second and third matrices is associated with deviatoric stress states. The eigenparameter c_2 is linked to the shear modulus [8]. The elastic parameters become

$$E = \frac{c_1 c_2}{c_1 + c_2} \quad \text{and} \quad \nu = \frac{c_1 - c_2}{c_1 + c_2}. \tag{52}$$

A linear transformation exists between $(c_{0.5}, c_0)$ and (c_1, c_2). The admissible domain for the parameters c_1 and c_2 is also defined by linear inequalities

$$\begin{bmatrix}1 & 0\\ -1 & 3\end{bmatrix}\begin{bmatrix}c_1\\ c_2\end{bmatrix} \succcurlyeq \underline{\mathbf{0}}. \tag{53}$$

For the sake of simplicity, if an equality constraint on the parameters c_1 and c_2 is chosen, it is the same as for the other parameterization (Equation (31)), i.e., $c_1 + c_2 = 1$.

C. Identification on the real experiments with the spectral parameterization

Identification results for the real experiments based on the interpolation parameterization were given in Section 4.3.1. This appendix presents the results obtained with the spectral parameterization (Figure 16). The EGM bias is also present, this time positive, as anticipated from the synthetic experiments. Only the results for images I_6 and I_7 are not pushed toward the maximum Poisson's ratio, which is consistent with the results obtained with the interpolation paramterization where the least biased results were also for images

I_6 and I_7 (Figure 10). The differences between REGM, SREGM and FEMU are more marked than with the interpolation parameterization, and the SREGM results are farther away from FEMU than those of REGM. This observation shows that, as expected, the link between REGM, SREGM, and FEMU results is reduced when the displacement residual cannot converge toward zero in the absence of measurement uncertainties because of model error. In addition, this result shows that when the displacement residual is large, SREGM has no guarantee of approximating FEMU compared with REGM.

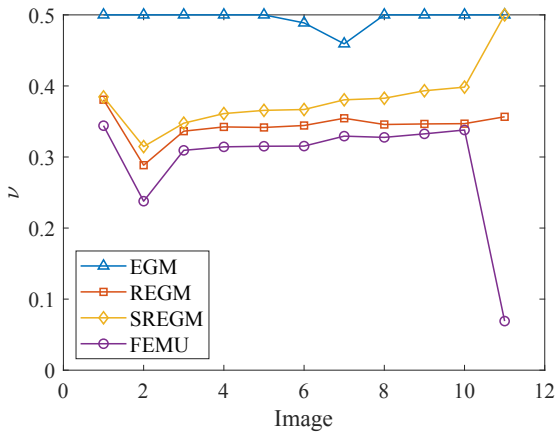

Figure 16: Identification results based on measured displacement fields using the spectral parameterization.

Figure 17 reports the displacement and image residuals for the identification based on the spectral parameterization. The residuals are similar to those obtained with the interpolation parameterization (Figure 11), except for EGM residuals, which are smaller with the spectral parameterization because the EGM bias is limited by the maximum value of ν equal to 0.5 which is close to 0.31 (i.e., the reference value).

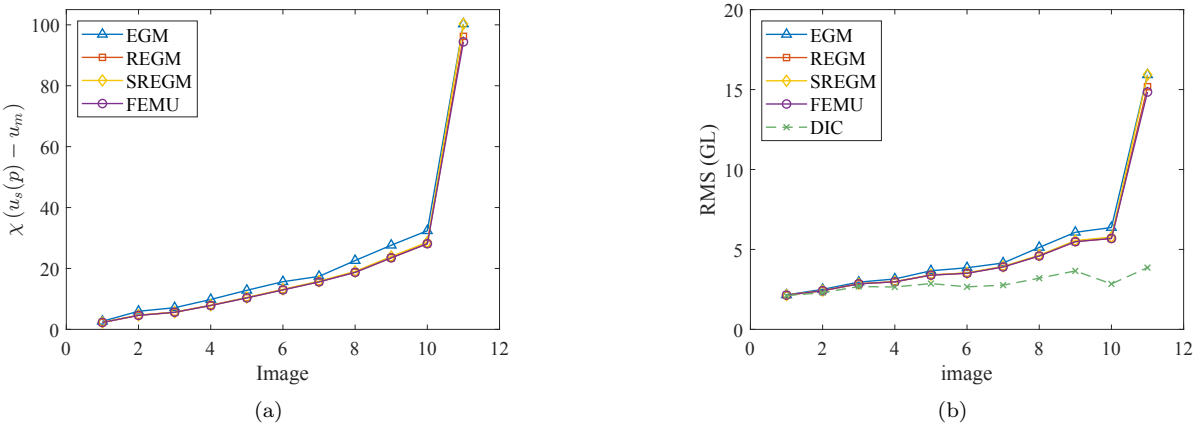

Figure 17: Errors in terms of displacements (a) and gray level (b) residuals for each image depending on the identification method using the spectral parameterization.

D. Gray level residuals for probing identification results

DIC allows displacement fields $\mathbf{u}$ to be measured by registering image I_k with respect to the reference image I_0. The pixel-wise residual r_k is defined as the gray level difference between that in the reference image $I_0(\mathbf{x})$ and that in the image of the deformed configuration I_k corrected by the measured displacement field $\mathbf{u}$

$$r_k(\mathbf{u},\mathbf{x}) = I_0(\mathbf{x}) - I_k\left(\mathbf{x}+\mathbf{u}(\mathbf{x})\right). \tag{54}$$

where $\mathbf{x}$ denotes any pixel position in the considered region of interest of DIC analyses. DIC estimates the displacement field by minimizing the root mean square (RMS) residual R_k

$$R_k^2(\mathbf{u}) = \frac{1}{N}\sum_{i=1}^{N} r_k\left(\mathbf{u},\mathbf{x}_i\right)^2 \tag{55}$$

where N is the number of pixels in the region of interest, and $\mathbf{x}_i$ the position of each pixel in the reference image. Global DIC encodes the displacement field on an FE mesh, denoted here $U_h(\Omega)$ [59, 60, 61].

To illustrate the gray level residuals (Equation (54)) obtained in DIC, two results are shown for the studied experiment. The gray level residuals are uniform for image I_6 (Figure 18(a)) and essentially reduce to acquisition noise. Conversely, the crack is clearly visible from the gray level residuals of the registration

of image I_{11} when $F = 11$ kN (Figure 18(b)). From these analyses, identifying the Poisson's ratio up to the end of the experiment is expected to be challenging because damage will create model errors if homogeneous elastic properties are sought.

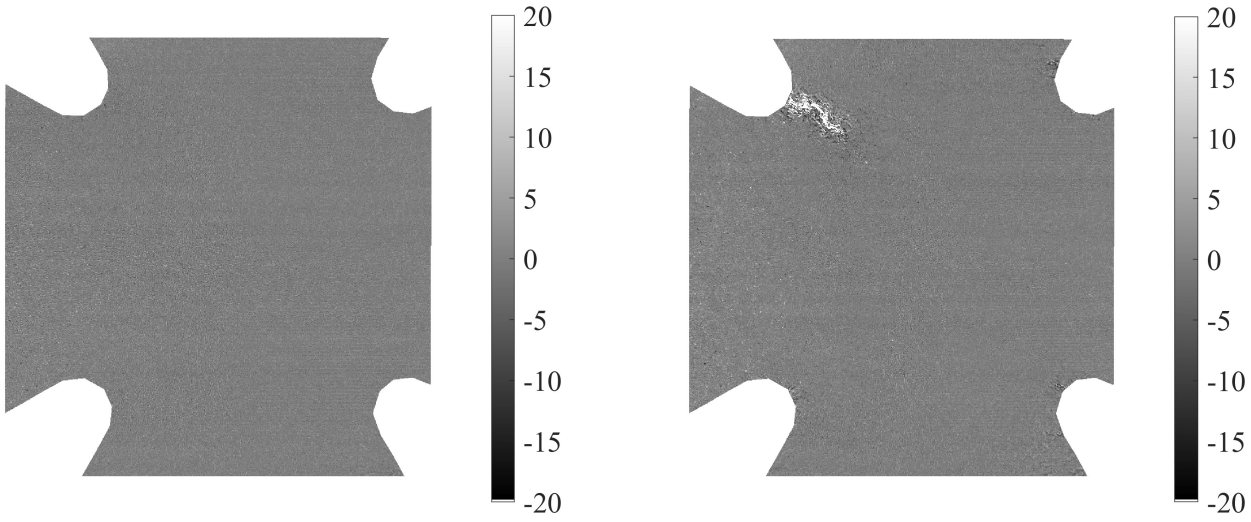

(a) (b)

Figure 18: Gray level residuals of the DIC analyses when $F = 6$ kN (a) and $F = 11$ kN (b). The dynamic range of the registered images is 8 bits.

For real experiments, images are available and DIC can be used to measure displacement fields by minimizing the RMS gray level residuals. The local gray level residuals r_k (Equation (54)) and their RMS level R_k (Equation (55)) can also be calculated with displacements obtained from FE simulations when driven by measured boundary conditions. The lower bound for the gray level residuals (for a specific mesh) is the one obtained from DIC, which directly minimizes its RMS. Comparing the gray level residuals for simulated displacements to the reference DIC residual gives insight into the relevance of any simulated displacement.